

TOI-4616 b: a benchmark Earth-sized planet transiting a nearby M4 dwarf

F. Zong Lang¹, B. O. Demory¹, Y. Gómez Maqueo Chew², Y. Schmid¹, M. Timmermans^{8,3}, F.J. Pozuelos²⁶, M. Gillon³, Artem Y. Burdanov¹⁴, Benjamin V. Rackham^{14,18}, D. Queloz^{6,33}, K.G. Stassun⁷, Khalid Barkaoui^{15,3}, Amaury Triaud^{3,13}, J. de Wit⁹, S. Zúñiga-Fernández¹², A. J. Burgasser²², Elsa Ducrot¹⁰, Madison G. Scott⁸, D. Sebastian^{9,10}, A. Soubkiou³, M. Lendl⁴, I. Plauchu-Frayn⁵, U. Schroffenegger¹, Erik Meier V.³², P. Pedersen^{6,3}, A. Khandelwal², Roman Gerasimov²⁴, C. Aganze²³, Chih-Chun Hsu²⁵, J.M. Jenkins²¹, Aishwarya R. Iyer²⁷, C. Watkins¹¹, C. A. Theissen²², K. A. Collins¹¹, H. P. Osborn²⁸, A. Shporer¹⁸, Claudia Janô Muñoz⁶, Toshi Suganuma³⁰, Norio Narita^{15,16,17}, Akihiko Fukui^{15,16}, F. Murgas^{15,29}, J. de Leon¹⁶, Enric Pallé^{15,29}, Yasmin Davis⁸, D. Kitzmann¹, Aishwarya R. Iyer²⁷, M. Pichardo Marcano², M.J. Hooton⁶

¹Center for Space and Habitability, University of Bern, Gesellschaftsstrasse 6, 3012, Bern, Switzerland

²Universidad Nacional Autónoma de México, Instituto de Astronomía, AP 70-264, CDMX 04510, México

³Astrobiology Research Unit, Université de Liège, Allée du 6 Août 19C, B-4000 Liège, Belgium

⁴Observatoire de l'Université de Genève, Chemin des Maillettes 51, CH-1290 Versoix, Switzerland

⁵Universidad Nacional Autónoma de México, Instituto de Astronomía, AP 106, Ensenada 22800, BC, México

⁶Cavendish Laboratory, JJ Thomson Avenue, Cambridge, CB3 0HE, UK

⁷Department of Physics & Astronomy, Vanderbilt University

⁸School of Physics and Astronomy, University of Birmingham, Edgbaston, Birmingham, B15 2TT, UK

⁹Massachusetts Institute of Technology, Cambridge, MA, USA

¹⁰LESIA Observatoire de Paris, Section de Meudon 5, place Jules Janssen 92195 MEUDON Cedex

¹¹Center for Astrophysics, Harvard & Smithsonian, Observatory Building E, 60 Garden St, Cambridge, MA 02138

¹²Département d'Astrophysique, ULiège, Belgique

¹³University of Birmingham, Birmingham, UK

¹⁴Department of Earth, Atmospheric and Planetary Science, Massachusetts Institute of Technology, 77 Massachusetts Avenue, Cambridge, MA 02139, USA

¹⁵Instituto de Astrofísica de Canarias (IAC), Calle Vía Láctea s/n, 38200, La Laguna, Tenerife, Spain

¹⁶Komaba Institute for Science, The University of Tokyo, 3-8-1 Komaba, Meguro, Tokyo 153-8902, Japan

¹⁷Astrobiology Center, 2-21-1 Osawa, Mitaka, Tokyo 181-8588, Japan

¹⁸Kavli Institute for Astrophysics and Space Research, Massachusetts Institute of Technology, Cambridge, MA, USA

¹⁹ETH Zurich, Zurich, Switzerland.

²⁰University of Harvard, Harvard, USA.

²¹NASA Ames Research Center, Moffett Field, CA 94035, USA

²²Department of Astronomy & Astrophysics, UC San Diego, La Jolla, CA 92093, USA

²³Kavli Institute for Particle Astrophysics & Cosmology, Stanford University, Stanford, CA 94305, USA

²⁴Department of Physics and Astronomy, University of Notre Dame, Nieuwland Science Hall, Notre Dame, IN 46556, USA

²⁵Center for Interdisciplinary Exploration and Research in Astrophysics (CIERA), Northwestern University, 1800 Sherman Ave, Evanston, IL, 60201, USA

²⁶Instituto de Astrofísica de Andalucía (IAA-CSIC), Glorieta de la Astronomía s/n, 18008 Granada, Spain

²⁷NASA Postdoctoral Fellow, NASA Goddard Space Flight Center, 8800 Greenbelt Road, Greenbelt, MD 20771, USA

²⁸Center for Space & Habitability, Physikalisches Institut, Universität Bern, Gesellschaftsstrasse 6, 3012 Bern, Switzerland

²⁹Inst. f. Teilchen- und Astrophysik, ETH Zürich, Wolfgang-Pauli-Strasse 27, 8093 Zürich, Switzerland

³⁰Departamento de Astrofísica, Universidad de La Laguna (ULL), E-38206 La Laguna, Tenerife, Spain

³¹Department of Multi-Disciplinary Sciences, Graduate School of Arts and Sciences, The University of Tokyo, 3-8-1 Komaba, Meguro, Tokyo 153-8902, Japan ³²Astrophysics

Accepted XXX. Received YYY; in original form ZZZ

ABSTRACT

Rocky exoplanets are particularly abundant around M-type stars. Their small radii and low luminosities provide favourable conditions for detecting transiting terrestrial planets and probing their atmospheric properties.

We report the discovery and statistical validation of TOI-4616 b, an Earth-sized planet transiting a nearby mid-M dwarf observed by TESS. We confirm the planetary nature of the signal and determine the system parameters by combining TESS photometry with ground-based multi-band transit observations, high-resolution imaging, and optical/near-infrared spectroscopy.

The host star lies at a distance of 28.10 ± 0.07 pc and has $R_{\star} = 0.1889 \pm 0.0096 R_{\odot}$, $M_{\star} = 0.1881 \pm 0.0094 M_{\odot}$, and $T_{\text{eff}} = 3150 \pm 75$ K. TOI-4616 b has a radius of $1.22 R_{\oplus}$ and an orbital period of 1.55 d. The planet receives an incident flux of $\sim 40 S_{\oplus}$, corresponding to an equilibrium temperature of ~ 525 K. This places TOI-4616 b in a regime intermediate between Earth-sized planets orbiting early M dwarfs and those around ultra-cool hosts.

Statistical validation with TRICERATOPS, supported by high-resolution imaging and chromatic transit constraints, yields a false-positive probability of 0.0135 below the recommended threshold of 0.015, confirming TOI-4616 b as a validated planet.

Due to its proximity to Earth, well-constrained stellar properties, and extensive multi-band follow-up, TOI-4616 b constitutes a valuable benchmark system for comparative studies of terrestrial planets around mid-M dwarfs and for future atmospheric investigations.

1 INTRODUCTION

The detection of terrestrial planets around mid-M dwarfs provides an empirical window into planet formation that cannot be gleaned from Solar System architectures alone (Chabrier et al. 2014; Chachan & Lee 2023). The relatively small radii and low luminosities of these stars enhance transit detectability and increase the amplitude of atmospheric spectral signatures (Dressing & Charbonneau 2013; Kreidberg 2015; Gratton 2025). Systems hosting short period terrestrial planets, such as the M-dwarf system GJ 1132 and its transiting planet GJ 1132 b illustrate how short-period, Earth-sized planets around cool hosts can serve as laboratories for atmospheric escape, photochemistry, and interior–atmosphere coupling (Libby-Roberts et al. 2022; Palle et al. 2025).

Over the past decade, the discovery and characterization of exoplanets has advanced rapidly, driven in large part by NASA’s Transiting Exoplanet Survey Satellite (TESS; Ricker et al. 2015). Among its detections is the nearby mid-M dwarf LP 466-156 (TIC 258796169; hereafter TOI-4616) with radius $0.1889 R_{\odot}$ and mass $0.1881 M_{\odot}$, around which a transiting planet candidate TOI-4616 b (also known as LP 466-156 b) with radius $1.22 R_{\oplus}$ and orbital period of 1.55 days was identified. While the existence of the candidate signal is well established from TESS photometry, its validation and detailed characterization require coordinated ground-based follow-up, spectroscopic analysis, and statistical vetting.

The statistical vetting of transiting exoplanet candidates has become a mature subfield in its own right. Comprehensive validation frameworks now combine stellar population synthesis, Galactic structure modeling, and priors for astrophysical false-positive scenarios to assess the probability that a candidate is genuinely planetary. Early validation efforts (Prša et al. 2011; Kochoska et al. 2017; Bray et al. 2025), developed for the Kepler mission, established the methodology for quantifying blend frequencies and background eclipsing binary rates. More recent tools such as VESPA (Mistry et al. 2023; Mantovan et al. 2022) and TRICERATOPS (Giacalone et al. 2020; Giacalone 2023) have expanded these techniques by incorporating multi-band transit depth constraints, high-resolution imaging limits, Gaia astrometry, and instrument-specific dilution corrections. In particular, TRICERATOPS, optimized for TESS targets, employs a hierarchical Bayesian framework to compute vetting probabilities and is especially well suited for M-dwarf systems where unresolved companions can complicate the interpretation of shallow transits.

A crucial component of this validation process is the exclusion of astrophysical false positives through complementary observational diagnostics. Multi-band transit photometry provides a decisive test: For genuine planetary transits, the depth is expected to be largely wavelength-independent across broad optical and near-infrared bands, aside from small variations introduced by atmospheric transmission features. In contrast, astrophysical false positives such as blended eclipsing binaries often produce strong chromatic transit depth variations (Mislis et al. 2010; Neckel 1995). Modern multi-band facilities routinely achieve the precision required to measure chromatic variations in transit depth (Narita et al. 2020), enabling the exclusion of blended eclipsing binaries via chromatic-depth analysis (Peláez-Torres et al. 2024; Ghachoui et al. 2024). Complementary high-resolution imaging further constrains the presence of bound or line-of-sight companions that may contaminate the photometry (Ziegler et al. 2021; Howell et al. 2021; Lester et al. 2021), thereby strengthening the statistical assessment of planetary authenticity.

Ground-based facilities optimized for faint red hosts, such as the SPECULOOS telescopes (Sebastian et al. 2021a, 2020; Delrez et al. 2018a), the SAINT-EX 1-m telescope in San Pedro Mártir

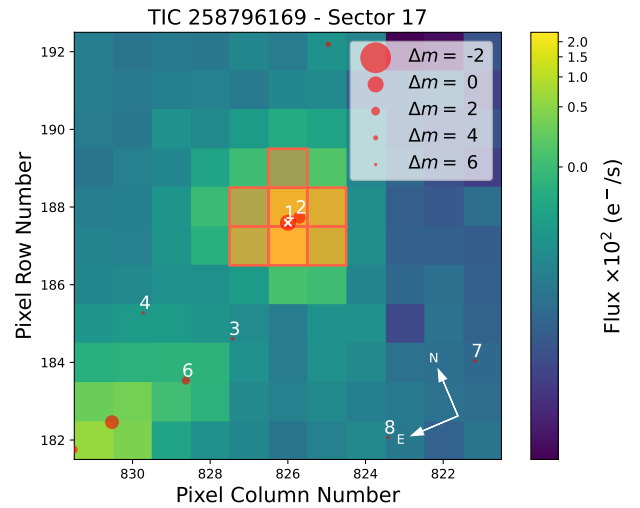


Figure 1. Target Pixel File (TPF) of TOI-4616 from TESS Sector 17. The color scale shows the median pixel flux. The red squares indicate the optimal photometric aperture used to extract the light curve. Nearby sources are marked and scaled according to their TESS magnitude difference relative to the target (Δm). A neighbouring star falls within the photometric aperture and contributes a small amount of contaminating flux, which is accounted for in the analysis. The figure was produced using TPFLOTTER (Aller et al. 2020).

(Demory et al. 2020), and MuSCAT2 at Teide Observatory (Narita et al. 2019) play an essential role in refining transit parameters, measuring chromatic effects, and strengthening statistical validation. When combined with spectroscopic characterization and Spectral Energy Distribution (SED) fitting, these observations enable a self-consistent determination of host-star properties and therefore of planetary parameters.

Owing to its proximity, well-constrained stellar properties, and the availability of extensive multi-instrument photometry and spectroscopy, TOI-4616 represents a valuable benchmark system for studies of terrestrial planets orbiting mid-M dwarfs. In this work we therefore present not only the confirmation of the planet but a comprehensive characterization of the system, with the goal of establishing TOI-4616 as a reference target for comparative studies of small planets around late-type stars with well-characterized host and extensive follow-up observations.

We present a comprehensive analysis of the TOI-4616 system that integrates the TESS discovery data (Sect. 2.1) with ground-based multi-instrument photometry (Sect. 2.2), high-resolution imaging (Sect. 3), and optical/near-infrared spectroscopy (Sect. 4) used for stellar characterization (Sect. 4.3). We adopt a uniform reduction and modeling framework, performing a joint transit analysis to derive the planet’s physical parameters (Sect. 5) and compute false-positive probabilities under a broad set of astrophysical scenarios (Sect. 7).

We conclude with a discussion of the broader implications of this system in Sect. 8.

2 OBSERVATIONS

2.1 TESS photometry

TOI-4616 is included in the revised TESS Input Catalog and candidate target list (Stassun et al. 2018) and was observed at 2-minute cadence in Sectors 17, 42, 43, and 70. We extracted the PDCSAP light curves from

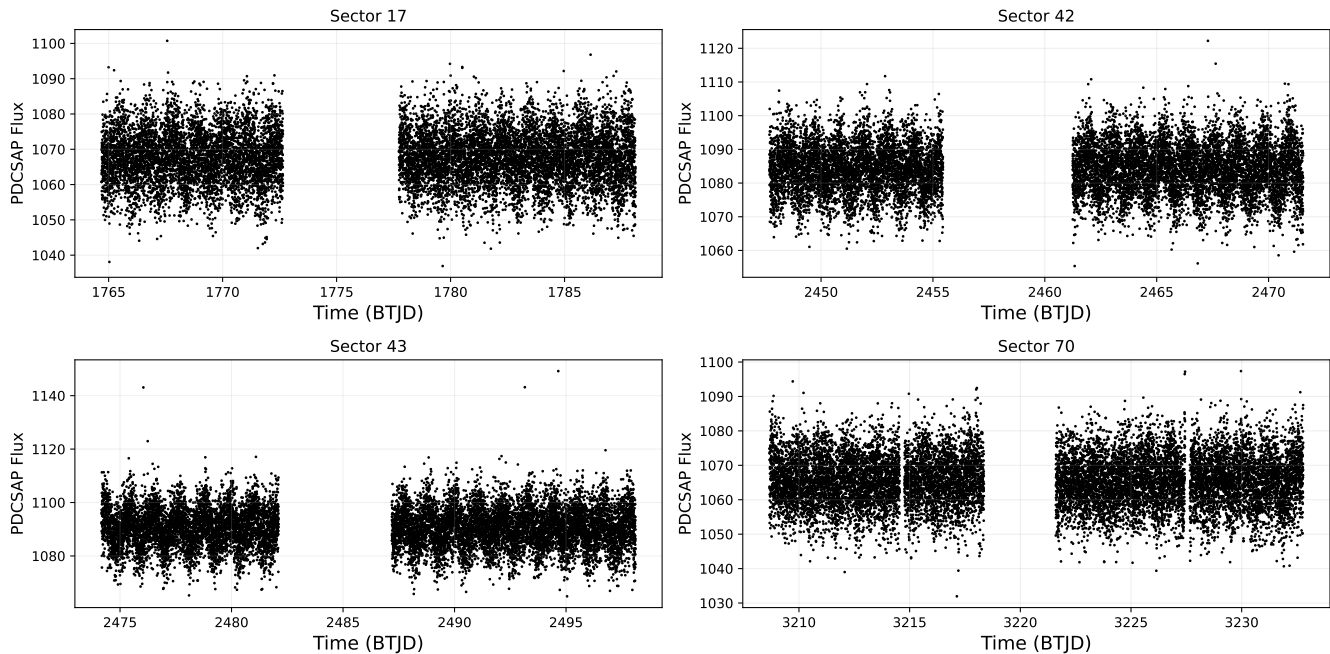


Figure 2. TESS PDCSAP light curves of TOI-4616 from Sectors 17, 42, 43, and 70. Each panel shows the flux time series for one sector, illustrating the sector-to-sector variation in photometric scatter and long-term systematics. Data gaps reflect the two-orbit observing strategy of TESS.

all available sectors using the `LightKurve` package¹ (LightKurve Collaboration et al. 2018). The sector light curves were stitched together, NaN values removed, and a 5σ clipping applied to reject outliers. The final dataset comprises more than 39000 photometric measurements and includes 68 transit events.

To reduce the computational cost of the joint transit analysis while preserving the information content of the data, we retained only measurements within ± 10 hours of each transit midpoint. This selection reduces the dataset to approximately 20000 points while maintaining full transit coverage and sufficient out-of-transit baseline.

The TESS light curve shows clear correlated variability, likely dominated by stellar rotation and instrumental systematics (Figure 3). To account for these effects, we model the photometry using a Gaussian Process (GP) 5.3 jointly with the transit model. All reported transit parameters are obtained while marginalizing over the GP hyperparameters in the global fit. For visualization purposes, we also display the GP-predicted variability and the corresponding detrended light curve.

2.2 Ground based photometry

2.2.1 SAINT-EX photometry

We observed TOI-4616 over seven nights with the 1-m SAINT-EX telescope at the San Pedro Mártir Observatory, Mexico, using the $I+Z$ on UTC 2021 November 13, 19, 27, 30, and UTC 2022 January 25 and i' bands on UTC 2024 October 09 and 20 with an exposure time of 30 s. Observations were conducted using the Astra observatory control software (Pedersen et al. 2023)².

Raw science frames were reduced using the SAINT-EX module of the PRINCE pipeline (Photometric Reduction and In-depth Nightly

Curve Exploration; Demory et al. 2020), which performs bias, dark, and flat-field corrections. The world coordinate system (WCS) solution was derived using `Astrometry.net` (Lang et al. 2010). Reference stars were identified using `Photutils` (Bradley et al. 2020), and differential photometry was extracted via aperture photometry.

To correct for common-mode systematics (i.e., time-dependent trends affecting all stars in the field, such as transparency and airmass variations), we applied a weighted principal component analysis (WPCA; Delchambre 2015; Wells et al. 2021) to the reference-star light curves. In this approach, each reference star is weighted by the inverse of its flux uncertainty, allowing the removal of shared trends while preserving astrophysical variability in the target light curve.

The resulting light curves exhibit significant correlated variability linked to stellar rotation and atmospheric systematics. We therefore modeled the data jointly with a Gaussian Process and transit model using the `juliet` framework, as illustrated in Fig. 5.

2.2.2 SPECULOOS-North/Artemis photometry

SNO/Artemis (Search for habitable Planets Eclipsing ULtra-cOOl Stars, Jehin et al. 2018; Delrez et al. 2018b; Sebastian et al. 2021b; Burdanov et al. 2022) observed a full transit of TOI-4616 b on UTC 2025 August 3 in the Sloan- z' filter with an exposure time of 12s. SNO/Artemis is equipped with a 2K \times 2K Andor iKon-L camera with a pixel scale of 0.35'', resulting in a field of view of 12' \times 12'. Data reduction and photometric analysis were performed using the `prose`³ pipeline (Garcia et al. 2022).

¹ <https://github.com/lightkurve>

² <https://github.com/ppp-one/astra>

³ Prose: <https://github.com/lgrcia/prose>

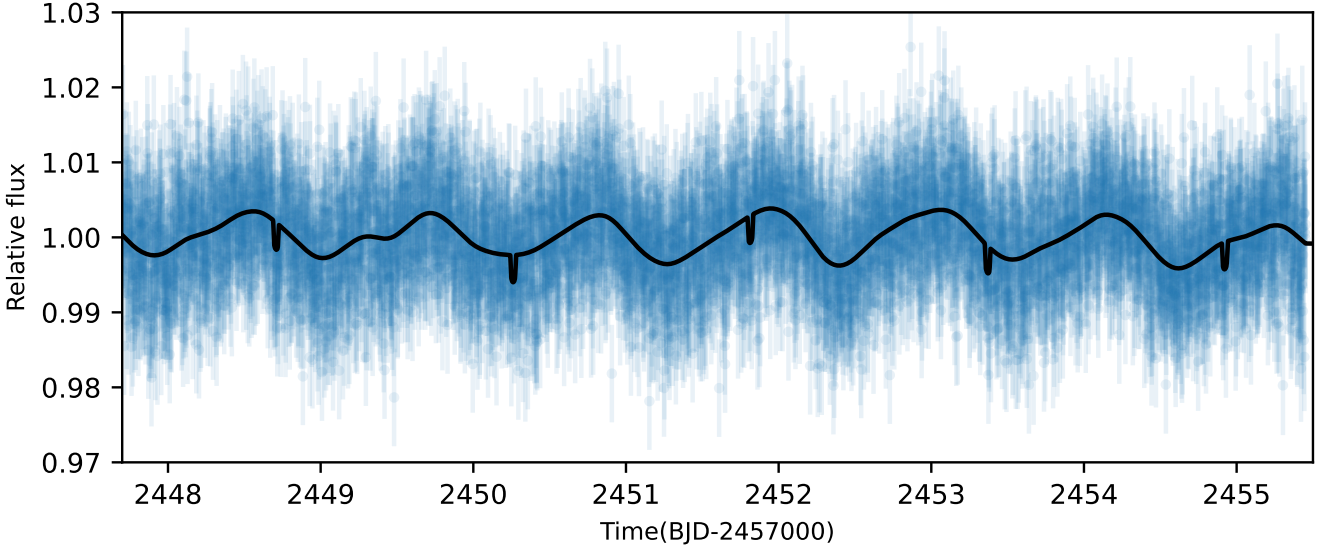


Figure 3. Section of the TESS light curve illustrating the intrinsic variability of the host star. Blue points show the photometric measurements, while the black curve represents the Gaussian Process model used to capture correlated variability.

Table 1. Ground-based photometric follow-up observations for TOI-4616.

Telescope (m)	Camera	Filter	Pixel scale ("/>pix)	Aperture (pix)	Coverage	Date	Duration (min)	Exposures
SAINT-EX (1.0)	Andor ikon-L	I+Z	0.35	7.5	Full transit	2021 Nov 13	339	423
SAINT-EX (1.0)	Andor ikon-L	I+Z	0.35	5.5	Full transit	2021 Nov 19	477	429
SAINT-EX (1.0)	Andor ikon-L	I+Z	0.35	5.5	Full transit	2021 Nov 27	421	525
SAINT-EX (1.0)	Andor ikon-L	I+Z	0.35	5.5	Full transit	2021 Nov 30	444	569
SAINT-EX (1.0)	Andor ikon-L	I+Z	0.35	5.5	Full transit	2022 Jan 25	172	156
LCO (2.0)	MuSCAT3	i'	0.27	5.1	Full transit	2022 Jan 15	564	188
LCO (2.0)	MuSCAT3	r'	0.27	5.1	Full transit	2022 Jan 15	480	160
LCO (2.0)	MuSCAT3	g'	0.27	5.1	Full transit	2022 Jan 15	189	63
LCO (2.0)	MuSCAT3	z_s	0.27	5.1	Full transit	2022 Jan 15	612	204
TCS-MuSCAT2 (1.52)	MuSCAT2	i'	0.44	4.0	Full transit	2021 Dec 05	237	456
TCS-MuSCAT2 (1.52)	MuSCAT2	r'	0.44	4.0	Full transit	2021 Dec 05	237	456
TCS-MuSCAT2 (1.52)	MuSCAT2	g'	0.44	4.0	Full transit	2021 Dec 05	237	238
TCS-MuSCAT2 (1.52)	MuSCAT2	z_s	0.44	4.0	Full transit	2021 Dec 05	177	321
LCOGT (1.0)	SINISTRO	i'	0.39	3.1	Full transit	2020 Mar 2	177	268
SAINT-EX (1.0)	Andor ikon-L	i'	0.35	8.0	Full transit	2024 Oct 09	211	189
SAINT-EX (1.0)	Andor ikon-L	i'	0.35	8.0	Full transit	2024 Oct 20	238	250
SNO/Artemis (1.0)	Andor ikon-L	z'	0.35	5.0	Full transit	2025 Aug 03	200	310

2.2.3 LCOGT photometry

We observed a full event window of TOI-4616 on UTC 2022 January 15 simultaneously in Sloan g' , r' , i' , and Pan-STARRS z -short from the Las Cumbres Observatory Global Telescope (LCOGT; Brown et al. 2013) 2 m Faulkes Telescope North at Haleakala Observatory on Maui, Hawai'i. The telescope is equipped with the MuSCAT3 multi-band imager (Narita et al. 2020). We also observed a full transit window on UTC 2021 December 09 from the LCOGT 1 m network node at Teide Observatory on the island of Tenerife (TEID). We used the TESS Transit Finder, which is a customized version of the Tapir software package (Jensen 2013), to schedule our transit observations. All images were calibrated by the standard LCOGT BANZAI pipeline (McCully et al. 2018) and differential photometric data were extracted using AstroImageJ (Collins et al. 2017a). We used circular photometric apertures of 5.1" (MuSCAT3) and 3.1" (TEID) that excluded the flux from the nearest known neighbor in the Gaia DR3 catalog (Gaia DR3 2777125789169639168), which

is 6.8" east of TOI-4616. The light curve data are available on the EXOFOP-TESS website⁴.

2.3 MuSCAT2 photometry and transit analysis

TOI-4616 was observed on UTC 2021 December 5, using the multi-band imager MuSCAT2 (Narita et al. 2019), mounted on the 1.5 m Telescopio Carlos Sánchez (TCS) at Teide Observatory, Spain. MuSCAT2 is equipped with four CCDs, enabling simultaneous imaging in the g' , r' , i' , and z_s bands with minimal readout time. Each CCD features 1024×1024 pixels, providing a field of view of 7.4×7.4 arcmin². Observations were conducted at the telescope's nominal focus, with exposure times set to 30 s for the g' , r' , and i' bands, and 15 s for the z_s channel. The raw data were processed using the

⁴ <https://exofop.ipac.caltech.edu/tess/target.php?id=258796169>

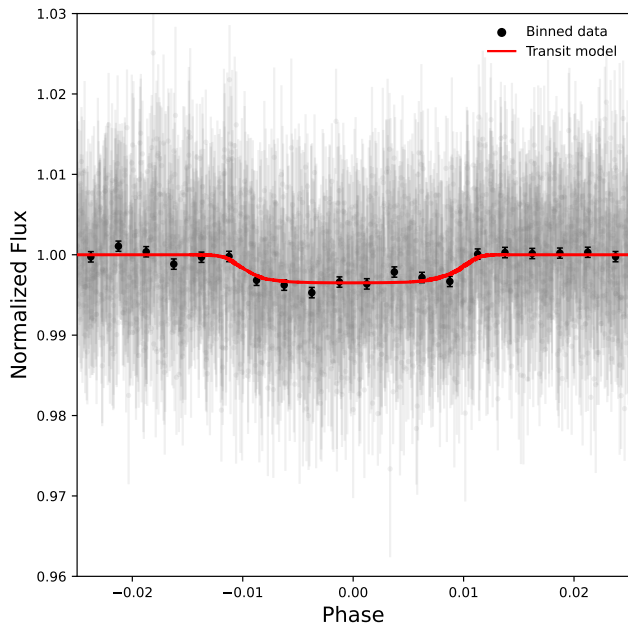


Figure 4. Phase-folded TESS light curve after variability modeling. The grey points show the GP-detrended photometry. The black points show the data binned into 300 uniform bins in orbital phase from the full set of 54 270 measurements. The red curve shows the transit model.

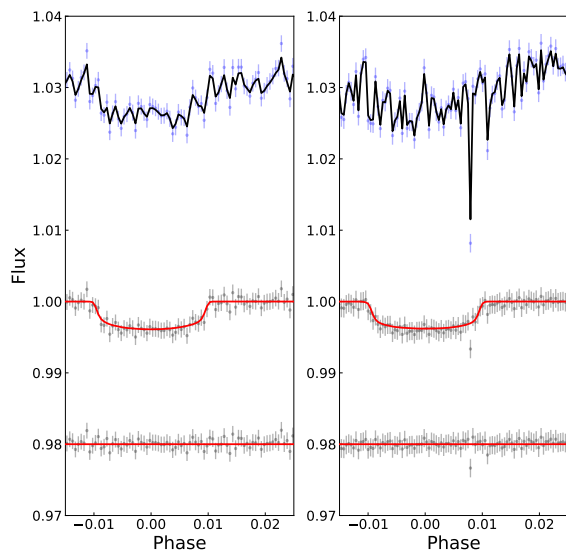


Figure 5. Recovery of the transit signal from highly variable SAINT-EX i' -band photometry obtained on UTC 2024 October 09 (left) and UTC 2024 October 20 (right). In each panel, the top sub-panel shows the raw light curve (black points) and the GP model (blue curve) capturing correlated variability and systematics. The middle sub-panel shows the GP-detrended light curve with the best-fit transit model overplotted (red). The bottom sub-panel shows residuals after removing both GP and transit components. Despite strong time-correlated variability in the raw photometry, the joint GP+transit model robustly isolates the transit signal. The GP modeling was performed within the `juliet` framework.

MuSCAT2 pipeline (Parviainen et al. 2019), which performs dark and flat-field calibrations, aperture photometry, and transit model fitting, including corrections for instrumental systematics.

The MuSCAT2 dataset exhibits strongly correlated noise associated with atmospheric variability and site-dependent systematics, which prevents a stable recovery of the transit depth under a purely parametric model. To appropriately capture the structure of this noise, we employ a Gaussian Process with a quasi-periodic covariance kernel. The periodic term is tied across filters via the stellar rotation period inferred from the TESS data set Fig. 3, while the amplitude and length-scale hyperparameters are allowed to vary per filter to account for wavelength-dependent systematics. This approach yields a physically realistic characterization of the noise and suppresses spurious depth variations that would otherwise mimic chromaticity. We propagated the uncertainty on d_{rot} by sampling it with a Gaussian prior in the GP model.

Under this GP model, the MuSCAT2 transit depth converges to $d = 0.049 \pm 0.012$, which is fully consistent with the depth obtained from TESS and the higher-precision ground-based instruments E1. Consequently, although MuSCAT2 does not independently constrain chromaticity, it provides a valuable corroborative dataset that is compatible with the planetary interpretation when treated with an adequate noise model.

In the MuSCAT2 i' observations, a single $> 8\sigma$ outlier was identified and removed prior to the joint fit. Its inclusion introduced a spurious pre-ingress trend, whereas its removal yields a flat baseline without affecting the inferred transit depth.

3 HIGH RESOLUTION IMAGING

3.1 Speckle imaging with NESSI at WIYN

We observed TOI-4616 on UTC 2021 December 21 using the NN-EXPLORE Exoplanet Stellar Speckle Imager (NESSI) (Scott et al. 2018), a speckle imager employed at the WIYN 3.5 m telescope on Kitt Peak. NESSI was used to obtain speckle images in a filter at $\lambda_c = 832$ nm. The observation consisted of a set of 9000 exposures each with a 40 ms exposure time. NESSI’s field-of-view was limited by using 256×256 pixel sub-array readouts, resulting in a $4.6'' \times 4.6''$ field. However, our speckle measurements were further confined to an outer radius of $1.2''$ from TOI-4616. Speckle imaging of a point source standard star was taken in proximity to the observation of TOI-4616 and consisted of a set of 1000 exposures used to calibrate the intrinsic PSF.

These speckle data were reduced using the pipeline process described in Howell et al. (2011). Among the pipeline products is a reconstructed image of the field around TOI-4616. We used this to measure contrast curves, setting detection limits on point sources close to the TOI-4616 host star. No companion sources were detected within $1.2''$ of the star brighter than the contrast limits, which reached 3.9 magnitudes at $0.2''$ and 5 magnitudes at $1''$ from the star.

4 STELLAR CHARACTERIZATION

4.1 Shane/Kast optical spectroscopy

We observed TOI-4616 with the Kast double spectrograph (Miller & Stone 1994) on the 3m Shane telescope at Lick Observatory on UTC 2021 November 27 in cloudy and windy conditions with $0''.9$ seeing. We used the $1''.5$ slit aligned to the parallactic angle to obtain blue and red optical spectra split at 5700 \AA by the d57 dichroic, and dispersed

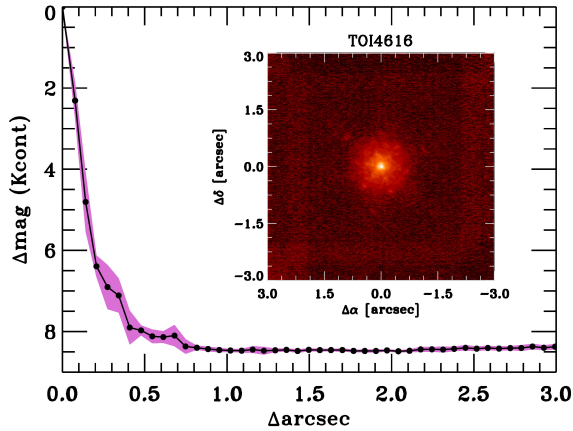


Figure 6. The contrast curve and the high-resolution image show the absence of any close companion.

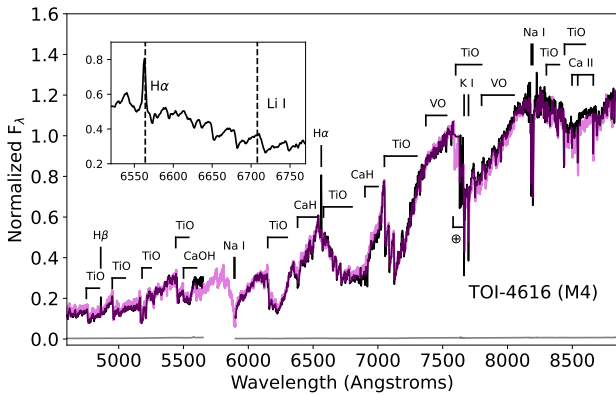


Figure 7. Blue and red Shane/Kast optical spectrum of TOI-4616 (black line) compared to the best-fit M4 SDSS spectral template from [Bochanski et al. \(2007\)](#), (magenta line). Key spectral features are indicated, including regions of strong telluric absorption (\otimes). The inset box shows the 6520–6770 Å region encompassing the strong 6563 Å H α emission line and absent 6708 Å Li I absorption.

by the 600/4310 grism and 600/7500 grating, resulting in spectral resolutions of $\lambda/\Delta\lambda \approx 1100$ and ≈ 1500 , respectively. We obtained a single 1200 s exposure in the blue channel and two 600 s exposures in the red channel at an average airmass of 1.10. The G5 V star HD 3266A ($V = 8.3$) was observed afterward at a similar airmass for telluric absorption calibration, and the spectrophotometric calibrator Feige 110 ([Hamuy et al. 1992, 1994](#)) was observed on the same night for flux calibration. HeHgCd and HeNeArHg arc lamp exposures were used to wavelength calibrate our blue and red data, and flat-field lamp exposures were used to correct for pixel response variation. Data were reduced using the `kastredux` code⁵ using standard settings. The resulting spectra have median signals-to-noise of 45 at 5425 Å and 167 at 7350 Å.

The reduced spectrum is shown in Fig. 7, and is compared to the best-fit M4 dwarf spectral template from [Bochanski et al. \(2007\)](#). This optical classification is consistent with that reported by [Kesseli et al. \(2019\)](#), and confirmed using index-based methods described in

[Reid et al. \(1995\)](#); [Gizis \(1997\)](#); [Martín et al. \(1999\)](#); [Lépine et al. \(2003\)](#); and [Riddick et al. \(2007\)](#) all of which yield M4 types. We detect strong 6563 Å H α and 4861 Å H β with equivalent widths of -3.80 ± 0.11 Å and -2.8 ± 0.3 Å, respectively. The former translates into a relative H α luminosity of $\log(L_{H\alpha}/L_{bol}) = -3.86 \pm 0.06$ using the χ factor relation of [Douglas et al. \(2014\)](#), well into the saturated regime. The presence of strong H α emission indicates an activity age $\lesssim 4.5$ Gyr ([West et al. 2008](#)) and possibly younger, although the absence of detectable 6708 Å Li I absorption rules out an age less than ~ 30 Myr. We measure a zeta metallicity index of $\zeta = 0.939 \pm 0.003$ ([Lépine et al. 2013](#)), corresponding to a solar metallicity ($[Fe/H] = -0.07 \pm 0.20$; [Mann et al. 2013a](#)), consistent with prior measurements from APOGEE ($[Fe/H] = -0.071 \pm 0.009$; [Sprague et al. 2022](#)).

4.2 IRTF/SpeX near-infrared spectroscopy

We observed TOI-4616 with the SpeX spectrograph ([Rayner et al. 2003](#)) on the 3.2-m NASA Infrared Telescope Facility (IRTF) on UTC 2021 December 24 and UTC 2024 October 7. Conditions were clear on both nights, with seeing of $1''.4$ and $1''.2$. In each visit, we used the short-wavelength cross-dispersed (SXD) mode of SpeX with the $0.3'' \times 15''$ slit aligned to the parallactic angle, which yields 0.80–2.42 μm spectra at a resolving power of $R \sim 2000$, and obtained six exposures while nodding in an ABBAAB pattern. Integration times were 180 s and 150 s per exposure. Each sequence was followed by SXD calibration frames and six short exposures of the A0 V standard HD 7215 ($V = 7.0$). Both datasets were reduced with `Spextool v4.1` ([Cushing et al. 2004](#)). The final spectra from 2021 and 2024, shown in Fig. 8, have median SNR per pixel values of 123 and 112, respectively, and an average of 2.5 pixels per resolution element.

We compared the SpeX spectra of TOI-4616 to M dwarf standards in the IRTF Spectral Library ([Cushing et al. 2005](#); [Rayner et al. 2009](#)) using the SpeX Prism Library Analysis Toolkit (SPLAT, [Burgasser & Splat Development Team 2017](#)), finding the best match to the M4 V standard Ross 47 on both nights. We therefore adopt an infrared spectral type of $M4.0 \pm 0.5$. Using SPLAT, we also measured the equivalent widths of the K-band Na I and Ca I features and the H 2O –K2 index ([Rojas-Ayala et al. 2012](#)). Applying the empirical relation of ([Mann et al. 2013b](#)), we derive nearly identical iron abundance estimates from the 2021 and 2024 observations. Taking the weighted mean of the two, we adopted a final metallicity of $[Fe/H] = -0.32 \pm 0.11$ dex, where the uncertainty reflects the systematic limit of the empirical relation.

4.3 Comprehensive characterization of the TOI-4616 system

To derive accurate stellar properties for TOI-4616, we combine photometric, spectroscopic, and astrometric constraints with empirical calibrations appropriate for mid-M dwarfs. In this section we present the derivation of the stellar mass, radius, effective temperature, luminosity, and metallicity, which form the basis for determining the planetary parameters.

4.3.1 Empirical Relations

We estimated the stellar parameters of TOI-4616 using the empirical relations of [Mann et al. \(2015, 2019\)](#). Based on the apparent K_s magnitude of the star ([Skrutskie et al. 2006](#)) and its Gaia DR3 parallax ([Gaia Collaboration et al. 2023](#)), we derive a mass of $0.1611 \pm 0.0037 M_{\odot}$. Incorporating the metallicity measured from the SpeX spectrum, we estimate a radius of $0.1969 \pm 0.0056 R_{\odot}$. These values

⁵ <https://github.com/aburgasser/kastredux>.

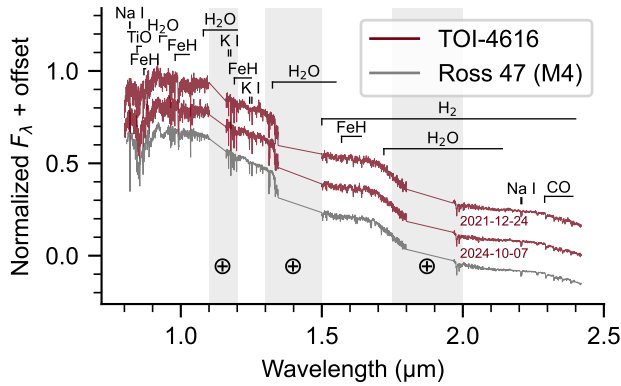


Figure 8. SpeX SXD spectra of TOI-4616 from 24 Dec 2021 (top) and 7 Oct 2024 (bottom). The target spectra (red) are shown alongside the M4V standard Ross 47 (grey), offset vertically for clarity. Prominent M-dwarf spectral features are labeled, and regions of strong telluric absorption are shaded.

yield a surface gravity of $\log g = 5.057 \pm 0.027$ (cgs). The Gaia $BP-RP$ color corresponds to an effective temperature of 3280 ± 77 K. Using the Stefan–Boltzmann Law, we calculate a bolometric luminosity of $0.00404 \pm 0.00044 L_{\odot}$.

4.3.2 SED Analysis

As an independent determination of the basic stellar parameters, we performed an analysis of the broadband SED of the star together with the *Gaia* DR3 parallax (with no systematic offset applied; see, e.g., [Stassun & Torres 2021](#)), to determine an empirical measurement of the stellar radius, following the procedures described in [Stassun & Torres \(2016\)](#); [Stassun et al. \(2017\)](#); [Stassun & Torres \(2018\)](#). We pulled the the JHK_S magnitudes from 2MASS, the W1–W3 magnitudes from WISE, the $G_{BP}G_{RP}$ magnitudes from *Gaia*, as well as the absolute flux-calibrated *Gaia* spectrophotometry. Together, the available photometry spans the full stellar SED over the wavelength range 0.4–10 μm (see Figure 9).

We performed a fit using PHOENIX stellar atmosphere models, with the free parameters being the effective temperature (T_{eff}) and metallicity ($[\text{Fe}/\text{H}]$), as well as the extinction A_V , which we fixed at zero due to the proximity of the TOI-4616 system to Earth. While model uncertainties exist for cool stellar atmospheres at longer wavelengths, PHOENIX models provide an adequate representation of the broadband spectral energy distributions of mid-M dwarfs for the purpose of estimating the bolometric flux (e.g., (?)). The resulting fit (Figure 9) has a best-fit $T_{\text{eff}} = 3150 \pm 75$ K, $[\text{Fe}/\text{H}] = -0.25 \pm 0.25$, with a reduced χ^2 of 1.3. Integrating the (unreddened) model SED gives the bolometric flux at Earth, $F_{\text{bol}} = 1.278 \pm 0.045 \times 10^{-10}$ $\text{erg s}^{-1} \text{cm}^{-2}$. Taking the F_{bol} and T_{eff} together with the *Gaia* parallax, gives the stellar radius, $R_{\star} = 0.1889 \pm 0.0096 R_{\odot}$. In addition, we can estimate the stellar mass from the empirical M_K relations of [Mann et al. \(2019\)](#), giving $M_{\star} = 0.1881 \pm 0.0094 M_{\odot}$.

We identified an unassociated bright star in the TESS photometric aperture, therefore, we also fitted its SED to estimate its contribution of contaminating flux to the TESS light curve of TOI-4616 ([Stassun et al. 2018](#); [Livingston et al. 2018](#); [Crossfield et al. 2016](#); [Mayo et al. 2018](#); [Collins et al. 2017b](#)). It is also represented in Figure 9, with the following best-fit parameters: $T_{\text{eff}} = 5250 \pm 100$ K, $A_V = 0.24 \pm 0.02$, and $[\text{Fe}/\text{H}] = -2.0 \pm 0.5$, with a resulting $R_{\star} = 5.8 \pm 1.0 R_{\odot}$.

The stellar parameters derived from the empirical relations of

Table 2. Basic information of TOI-4616. Stellar density $\rho_{\star, \text{SED}}$ is computed from the quoted M_{\star} and R_{\star} ; the transit-inferred density $\rho_{\star, \text{tr}}$ is reported separately in Table 3.

Parameter	Value	
<i>Main identifiers</i>		
TOI	4616	
TIC	258796169	
Gaia ID	2777125789169639296	
<i>Equatorial coordinates</i>		
RA (J2000)	00:59:16.34	
Dec (J2000)	+13:51:38.86	
<i>Photometric properties</i>		
TESS (mag)	12.8872 ± 0.0074	TIC V8 ^a
Gaia G (mag)	14.1881 ± 0.0006	Gaia DR3 ^b
Gaia BP (mag)	15.814 ± 0.004	Gaia DR3
Gaia RP (mag)	13.538 ± 0.002	Gaia DR3
B (mag)	15.83 ± 0.031	APASS
V (mag)	14.753 ± 0.039	APASS
J (mag)	11.317 ± 0.029	2MASS
H (mag)	10.713 ± 0.033	2MASS
K (mag)	10.47 ± 0.02	2MASS
WISE 3.4 μm (mag)	10.235 ± 0.022	WISE
WISE 4.6 μm (mag)	10.018 ± 0.019	WISE
WISE 12 μm (mag)	9.862 ± 0.052	WISE
WISE 22 μm (mag)	8.652	WISE
<i>Astrometric properties</i>		
π (mas)	35.5096 ± 0.0302	Gaia DR3
μ_{α^*} (mas yr ⁻¹)	31.509 ± 0.036	Gaia DR3
μ_{δ} (mas yr ⁻¹)	179.276 ± 0.025	Gaia DR3
<i>Derived parameters</i>		
Distance (pc)	28.17 ± 0.02	This work (Gaia DR3)
M_{\star} (M_{\odot})	0.1881 ± 0.0094	This work
R_{\star} (R_{\odot})	0.1889 ± 0.0096	This work
$\log g$ (cgs)	4.70 ± 0.03	This work
ρ_{\star} (ρ_{\odot})	28.0 ± 4.5	This work
SpT	M4 \pm 0.5	This work
T_{eff} (K)	3150 ± 75	This work
F_{bol} ($\text{erg s}^{-1} \text{cm}^{-2}$)	$(1.28 \pm 0.05) \times 10^{-10}$	This work
[Fe/H]	-0.32 ± 0.11	SpeX (adopted)
	-0.25 ± 0.25	SED
	-0.071 ± 0.009	APOGEE
P_{rot} (days)	1.2	This work
Estimated age (Gyr)	0.3 – 0.8	This work

^aTIC V8, ^bGaia DR3 ([Gaia Collaboration et al. 2021](#)).

[Mann et al. \(2015, 2019\)](#) and from the SED analysis are broadly consistent within the expected systematic uncertainties of empirical calibrations for mid-M dwarfs. In the remainder of this work we adopt the SED-based stellar parameters, which incorporate the measured bolometric flux and Gaia parallax and therefore provide a direct empirical constraint on the stellar radius.

Integrating its SED gives a ratio of its flux in the TESS bandpass to that of TOI-4616 of 0.391 ± 0.017 .

We obtained multiple metallicity estimates for TOI-4616 from independent methods. The broadband SED fit provides only a weak constraint on $[\text{Fe}/\text{H}]$, as metallicity is partially degenerate with effective temperature and model assumptions in cool stellar atmospheres. The APOGEE pipeline yields a near-solar metallicity with very small formal uncertainty; however, the APOGEE pipeline uncertainties for mid-M dwarfs can be underestimated due to model and calibration systematics in this regime ([Passegger et al. 2022](#)). From the SpeX spectrum, we derive a metallicity using empirical near-infrared M-dwarf relations, which rely on metallicity-sensitive spectral features and are specifically optimized for late-type stars ([Lindgren et al. 2016](#)). Because these calibrations are tailored to M dwarfs and provide a

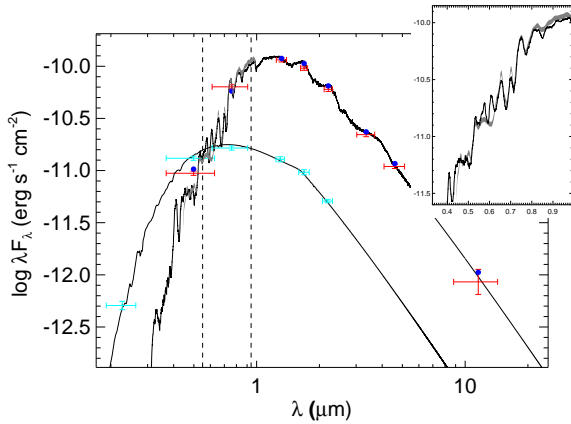


Figure 9. Spectral energy distribution of TOI-4616. Red symbols represent the observed photometric measurements, where the horizontal bars represent the effective width of the passband. Blue symbols are the model fluxes from the best-fit PHOENIX atmosphere model (black). The *Gaia* spectrophotometry is represented by the grey swathe, also shown in greater detail in the inset plot. An unassociated bright star in the TESS photometric aperture is represented by the light blue data points and associated fitted SED model, with which we estimate the contaminating flux in the light curve of TOI-4616; see the text.

physically motivated estimate, we adopt the SpeX-based metallicity as our fiducial value in the remainder of the analysis, while the APOGEE and SED values are treated as consistency checks. In the following sections, we therefore adopt the SpeX-based metallicity of $[\text{Fe}/\text{H}] = -0.32 \pm 0.11$ as the fiducial stellar metallicity.

The M4 dwarf TOI-4616 exhibits strong $\text{H}\alpha$ emission ($\text{EW} = -3.80 \pm 0.11 \text{ \AA}$);

$$\log(L_{\text{H}\alpha}/L_{\text{bol}}) = -3.86 \pm 0.06$$

but no detectable 6708 \AA Li I absorption (see Sect. 3). Combined with the rapid rotation of the star ($P_{\text{rot}} \approx 1.2 \text{ d}$) and the absence of a close companion, these indicators suggest a relatively young system. We therefore estimate an age of roughly 0.3–0.8 Gyr, though we note that age determinations for mid-M dwarfs remain intrinsically uncertain.

5 MODELING OF THE TRANSIT SYSTEM

5.1 Transit Model and Implementation

We modeled the transit light curves using the BATMAN package (Kreidberg 2015), which implements the analytical transit formalism of Mandel & Agol (2002). Exploration of the posterior parameter space was performed using the affine-invariant Markov Chain Monte Carlo sampler EMCEE (Foreman-Mackey et al. 2013).

5.2 Limb Darkening Treatment

We adopted a quadratic limb-darkening law (Mandel & Agol 2002). To construct informative priors on the limb-darkening coefficients, we used the LDTK toolkit (Parviainen & Aigrain 2015), which interpolates PHOENIX stellar atmosphere models (Husser et al. 2013) to compute filter integrated intensity profiles. The wavelength ranges of each instrument’s filter were supplied to LDTK together with the adopted stellar parameters of TOI-4616 ($T_{\text{eff}} = 3150 \text{ K}$, $\log g = 5.0$, $[\text{Fe}/\text{H}] = -0.32$). The resulting Gaussian priors on the coefficients (u_1, u_2) were used in the transit modeling.

Because TOI-4616 b has an orbital period of only 1.55 d, tidal

circularization is expected to be efficient. Observational studies show that short-period planets typically exhibit eccentricities consistent with zero, particularly when the data do not constrain small deviations from circularity. We therefore fixed the eccentricity to zero in the transit modelling, as allowing it to float is not justified by the data and may introduce biases in derived system parameters (Hadden & Lithwick 2014; Eyles et al. 2019; Shporer et al. 2014).

5.3 Noise Modeling and Gaussian Processes

Each dataset was modeled jointly with a Gaussian Process (GP) noise component to account for correlated systematics and stellar variability. The GP was implemented using the SHOTerm kernel from the *celerite* package (Foreman-Mackey et al. 2017), which describes correlated variability as a stochastically driven damped harmonic oscillator.

The GP and transit model were fitted simultaneously. The GP component captures correlated noise and variability, while the transit parameters are inferred marginalizing over the GP hyperparameters.

5.4 Multicolor Transit Fitting

To investigate possible wavelength-dependent variations in transit depth, we allowed R_p/R_\star to vary independently for each dataset. The impact parameter was constrained to physically meaningful values ($0 \leq b \leq 1 + R_p/R_\star$). For numerical stability, we parameterized b through its absolute value to prevent unphysical negative solutions without altering the transit geometry.

Figure 10 shows the phase-folded light curves and the median joint-fit model for all instruments. Small apparent differences in transit depth between datasets arise from photometric noise, filter-dependent systematics, and finite signal-to-noise ratios, and are consistent with the posterior uncertainties. We find no statistically significant wavelength-dependent variation in transit depth.

5.4.1 Radius ratio sampling

We extracted the posterior samples of the planet-to-star radius ratio, R_p/R_\star , from the joint multi-instrument fit shown in Fig. 10. The planet-to-star radius ratio distributions are shown in Fig. 11. In this fit, the transit depth was allowed to vary independently for each dataset in order to capture potential chromatic effects and instrument-dependent systematics.

To obtain a representative global radius ratio, we combined the posterior samples from all eight datasets and constructed the aggregated posterior distribution shown in Fig. 12. Because the datasets were fitted simultaneously within a joint Bayesian framework, the resulting global posterior reflects the radius ratio consistent with all datasets and therefore provides a tighter constraint than any individual dataset alone. From this distribution, we derive a median value of:

$$R_p/R_\star = 0.06009^{+0.00109}_{-0.00115}$$

where uncertainties correspond to the 16th and 84th percentiles. Because the transit depth was allowed to vary independently for each dataset, the combined posterior should be interpreted as an instrument-marginalized estimate of R_p/R_\star , which captures both statistical uncertainty and any residual inter-dataset systematics. We verified that the individual posteriors overlap within their credible intervals and that no statistically significant chromatic trend is present; the combined posterior is therefore used only as a representative global value.

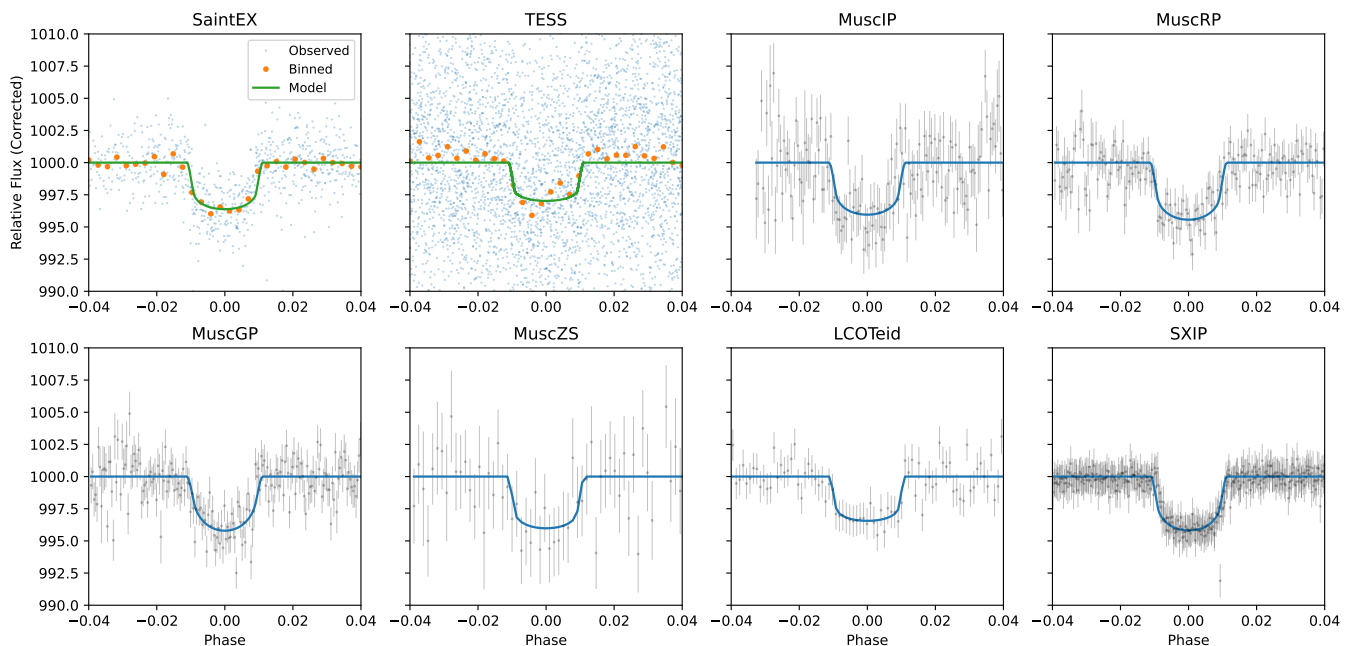


Figure 10. Phase-folded transit light curves and best-fit joint model for all available datasets: SAINT-EX, TESS, and the four MuSCAT3 filters (g' , r' , i' , z'). All panels are shown on identical phase and flux scales to allow direct comparison of transit depths. The solid line represents the median joint-fit model, while points show the observed data (with binning applied to the high-cadence SAINT-EX and TESS light curves for clarity). The SXIP panel represents observations with the SAINT-EX telescope in i-filter

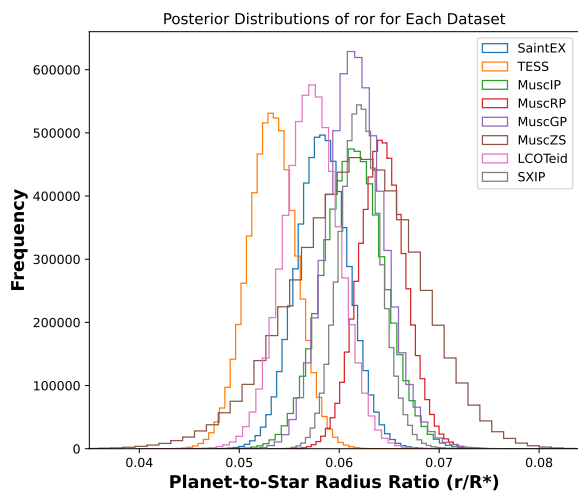


Figure 11. This figure shows the posterior distributions of the effective radius ratio for the six different filters used in our model.

6 THE SEARCH FOR ADDITIONAL PLANETS IN THE SYSTEM

During our extended ground-based monitoring of TOI-4616, observations obtained with the SNO/Ganymede telescope on UTC 2021 November 20 revealed a transit-like feature that does not correspond to the ephemeris of TOI-4616 b (Fig. 13). The signal is visible in the raw differential photometry and remains present after detrending. The data were corrected for instrumental systematics using the PRINCE pipeline and independently reduced with AstroImageJ (Collins et al.

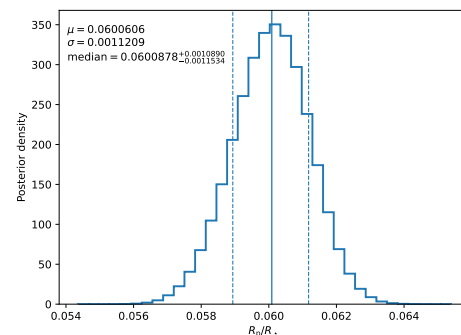


Figure 12. Posterior distribution of the planet-to-star radius ratio, R_p/R_* , obtained from the joint multi-instrument fit in which the transit depth was allowed to vary independently for each dataset (to capture potential chromatic effects). The distribution corresponds to the global posterior derived from the simultaneous fit to all datasets. The solid vertical line marks the posterior median, while the dashed lines indicate the 16th and 84th percentiles. The width of the distribution reflects the combination of statistical uncertainties and inter-instrument (and/or wavelength-dependent) depth variations.

2017a), yielding consistent light-curve features in the two independent reductions.

However, the event occurs near the end of the observing sequence, where correlations with airmass and other systematics increase and the photometric scatter rises. To quantify this behaviour, we computed a running RMS of the detrended residuals using a sliding window, which shows a clear increase in correlated noise toward the end of the sequence (Fig. 13c). Independent reductions and tests with different sets of reference stars yield broadly consistent results, indicating that the feature is not obviously introduced by a particular reduction choice. Nevertheless, because it coincides with less favourable observing conditions—where increasing sky background and atmospheric

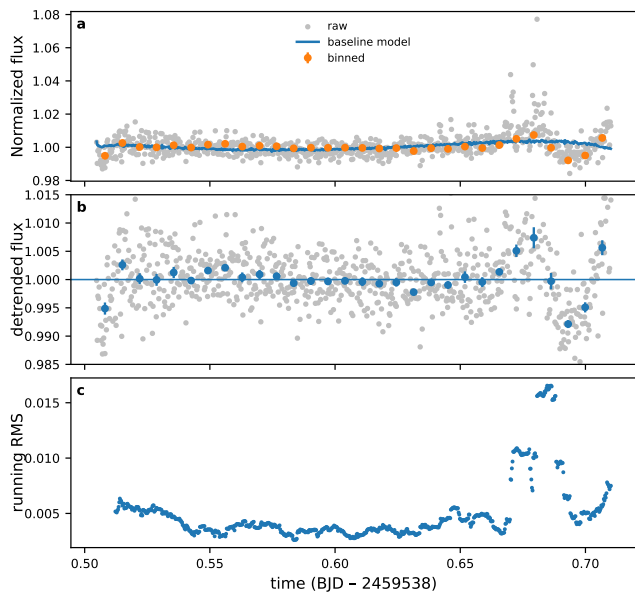


Figure 13. Ground-based photometry of TOI-4616 obtained with SNO/Ganymede on UTC 2021 November 20. (a) Raw differential flux and baseline model used for detrending. (b) Detrended light curve showing a shallow flux dip near the end of the observing sequence. (c) Running RMS of the detrended data, revealing a strong increase in correlated noise at the same time. The coincidence of the flux dip with the rise in photometric scatter suggests that the feature may be influenced by evolving systematics rather than a genuine transit.

variations can degrade photometric precision—its reliability remains uncertain. We therefore consider the feature suggestive but inconclusive. No other transit-like features were detected in our ground-based monitoring.

If interpreted as a planetary transit, the late-sequence flux dip in the SNO/Ganymede light curve has an approximate duration of $\sim 1\text{--}1.3$ h. For a planet orbiting TOI-4616 and assuming a circular orbit and near-central transit geometry, such a duration would correspond to an orbital period of order a few days ($\sim 2\text{--}5$ d), given the stellar density derived in Sect. 4.3. However, the event occurs near the end of the observing sequence, where correlations with airmass increase and the photometric scatter rises. The coincidence of the dip with increased correlated noise, as indicated by the running RMS analysis (Fig. 13), suggests that the feature is more plausibly associated with evolving systematics than with a genuine transiting signal.

Because the origin of this feature remains unclear, we analysed the TESS photometry to search for additional planets that could explain it. We used the SHERLOCK pipeline (Pozuelos et al. 2020; Dévora-Pajares et al. 2024), which is designed to identify planetary candidates that may be missed by standard detection pipelines such as SPOC or QLP (see, e.g., Dransfield et al. 2024; Zúñiga-Fernández et al. 2025; Yalçınkaya et al. 2025). We performed two independent searches: one using 120 s data from sectors 17, 42, 43, and 70, and another using 200 s data from sectors 42 and 43. In both cases, we recovered the signal corresponding to TOI-4616.01, confirming its detectability. No additional planetary candidates were identified.

To further quantify our sensitivity to additional planets, we performed an injection–recovery analysis using the MATRIX code⁶

⁶ MATRIX (Multi-phAse Transits Recovery from Injected eXoplanets) is available at <https://github.com/PlanetHunters/tkmatrix>

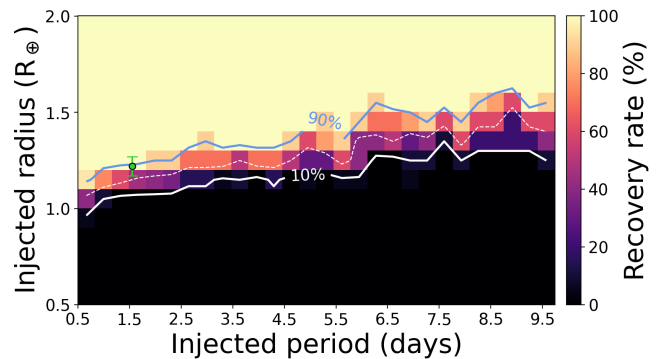


Figure 14. Results of the injection–recovery experiment conducted with MATRIX. The colour scale represents the recovery rate, with bright yellow indicating high recovery and dark purple/black indicating low recovery. The solid blue line marks the 90% recovery contour, the dashed white line the 50%, and the solid white line the 10%. The green dot marks the nominal value for TOI-4616 b.

(Dévora-Pajares & Pozuelos 2022). This framework explores the detection limits of the TESS data as a function of orbital period and planetary radius (see, e.g., Wells et al. 2021; Schanche et al. 2022; Pozuelos et al. 2023).

We constructed a grid of 30 orbital periods (0.5–10 d), 30 planetary radii ($0.5\text{--}3 R_{\oplus}$), and 10 transit epochs, yielding 9 000 injected scenarios. For each case, a synthetic transit signal was injected into the original 120 s TESS light curve and analysed after detrending with a bi-weight filter using a window size of 0.3 d, which was found to be optimal during the SHERLOCK exploration. A planet was considered successfully recovered if the detected period and epoch deviated by less than 1% and 1 hour, respectively, from the injected values.

The results are shown in Fig. 14. We identify a transition region where the recovery rate reaches 50%; this threshold shifts from about $1 R_{\oplus}$ at an orbital period of 0.5 d to roughly $1.3 R_{\oplus}$ at 10 d. Planets smaller than $1 R_{\oplus}$ remain essentially undetectable across the explored period range, with recovery rates below 10%. In contrast, planets larger than $1.5 R_{\oplus}$ are recovered with efficiencies above 80%, allowing us to confidently rule out their presence.

These limits indicate that any additional transiting companion consistent with the ground-based feature would likely have a radius below $\sim 1 R_{\oplus}$ and therefore remain challenging to detect in the current TESS data.

6.1 Transit Timing Variations (TTV)

We measured individual mid-transit times for both the TESS and ground-based light curves while fixing the transit shape to the global solution. The resulting timing residuals are consistent with a linear ephemeris within uncertainties, and we find no evidence for significant TTVs in the current dataset. The timing analysis is shown in Appendix F.

7 VALIDATION OF THE PLANETARY NATURE OF THE OBJECT

7.1 Statistical validation

We performed the statistical validation of TOI-4616 b using the TRICERATOPS⁷ package (Giacalone et al. 2021), a Bayesian framework to evaluate the probability of the planet hypothesis. It does so by testing a variety of possible astrophysical origin scenarios for the transit event and calculating their relative probabilities based on the flux of nearby stars. The planetary hypothesis is then evaluated by the false positive probability (FPP), and the nearby false positive probability (NFPP): a planet is considered statistically validated if it has an $FPP < 0.015$ and an $NFPP < 10^{-3}$.

We performed an initial analysis using the four sectors of TESS data available (17,42,43,70). First, we removed the stellar variability signal using the *wotan*⁸ package (Hippke et al. 2019). We selected a window size of 0.18 for the bi-weight filter to ensure that no transit feature is removed, and we computed an FPP of 0.823 and NFPP of 0.74. These probabilities are dominated by nearby eclipsing binary (NEB) and nearby transiting planet (NTP) scenarios around the closest neighboring star (TIC 258796170), which lies in the same pixels in TESS. We repeated the analysis with uncontaminated ground-based photometry, where a much smaller aperture was used to extract the target flux. Excluding the flux of the neighboring star removes the possibilities of NEB and NTP scenarios, effectively setting the NFPP to 0. By combining the contrast curve obtained from high-resolution imaging (see Section 3.1) and the phase-folded light curve obtained in the Sloan-*i'* filter (Section 2.2), the FPP was also reduced to 0.0135. These FPP and NFPP values are below the recommended thresholds (0.001 for NFPP and 0.015 for the FPP), and we can confidently classify TOI-4616 b as a validated planet.

7.2 Archival images

We used the archival images for TOI-4616 to exclude any possible background stars that could be blended with our target at its current position. TOI-4616 has a proper motion of 182 mas/yr. We used the data from POSS-I in 1954 and POSS-II in 1990 in the red filter, and PanSTARRS in 2011 and SNO/Artemis in 2025 in the z' filter, spanning a period of 71 years. The target has moved by $\sim 12.9''.4$ from 1954 to 2025. Fortunately, no background star object is detected in the current position of TOI-4616 (see Fig. 15).

8 DISCUSSION AND CONCLUSIONS

TOI-4616 b resides in an extreme irradiation environment for an Earth-sized planet orbiting a mid-M dwarf. This makes it a particularly informative test case for models of atmospheric escape, interior composition, and volatile retention.

The combination of precise stellar parameters, consistent multi-band transit measurements, and the host star's brightness makes TOI-4616 a particularly valuable system for future atmospheric and dynamical studies. We therefore highlight this system as a benchmark terrestrial planet orbiting a mid-M dwarf, well-suited for comparative investigations of planetary structure and evolution in the strongly irradiated regime.

⁷ <https://github.com/stevengiacalone/triceratops/tree/master>

⁸ <http://github.com/hippke/wotan>

8.1 Mass-radius relation and escape velocity

With a J-band magnitude of $J = 11.317 \pm 0.029$, TOI-4616 is accessible to high-precision near-infrared radial-velocity spectrographs optimized for mid-M dwarfs (Donati et al. 2018). Adopting a rocky mass–radius relation (Chen & Kipping 2017), we estimate a planetary mass of $M_p \approx 1.5\text{--}3.0 M_\oplus$, implying a radial-velocity semi-amplitude of $K \approx 2.5\text{--}4.0 \text{ m s}^{-1}$ (Suárez Mascareño et al. 2017).

High-precision near-infrared spectrographs such as CARMENES (Schöfer 2021), SPIRou (Karnavas 2024), IRD, and NIRPS (Artigau et al. 2024) are designed to achieve meter-per-second precision on mid-M dwarfs of similar brightness, suggesting that a mass determination may be feasible with an intensive monitoring campaign.

We performed Monte Carlo simulations to assess detectability. Assuming a semi-amplitude of 4.0 m s^{-1} , per-epoch precision of 3.5 m s^{-1} , and uniformly distributed observations over a 20-day baseline, we recover the signal at $\sim 3.7\sigma$ with 20 epochs and $\sim 5.7\sigma$ with 50 epochs. These estimates represent optimistic limits, as they do not include additional stellar variability.

The star's rapid rotation ($P_{\text{rot}} \approx 1.2 \text{ d}$ inferred from the quasi-periodic timescale of the Gaussian-process model fitted to the TESS light curve) likely implies significant magnetic activity and RV jitter at the several m s^{-1} level on timescales comparable to the orbital period (1.55 d). Disentangling planetary and activity signals will therefore require a substantial number of observations combined with activity diagnostics and joint modeling. We conclude that a precise RV mass measurement is challenging but potentially achievable with current facilities at the cost of significant telescope time.

8.2 Placement in the cosmic shoreline

TOI-4616 b lies in the high-irradiation, high-escape-velocity regime of the empirical cosmic shoreline (Ji et al. 2025; Meni-Gallardo & Pallé 2025). Using the posterior distribution of the planetary radius and a rocky mass–radius relation, we estimate the planetary mass and compute the escape velocity as

$$v_{\text{esc}} = \sqrt{2GM_p/R_p}$$

, yielding

$$v_{\text{esc}} = 14.9_{-4.5}^{+6.4} \text{ km s}^{-1}$$

Accounting for both bolometric instellation and stellar activity, we estimate the historical XUV irradiation using empirical activity–XUV scaling relations, obtaining

$$J_{\text{XUV}}/J_\oplus = (4.0 \pm 0.5) \times 10^3.$$

with activity level

$$\log\left(\frac{L_{\text{H}\alpha}}{L_{\text{bol}}}\right) = -3.86 \pm 0.06.$$

A schematic comparison of equilibrium temperature and irradiation regimes for short-period rocky planets is shown in Appendix D (Fig. D1).

The planet therefore, lies in a region where primordial H/He envelopes are expected to be efficiently stripped, while compact secondary atmospheres may survive (like GJ 486 b, see Fig. 17) (Misener & Schlichting 2021). Any present atmosphere is thus likely to be high-mean-molecular-weight (e.g. CO₂, N₂) or continuously replenished (Caldiroli et al. 2021; Teske et al. 2025).

Interestingly, TOI-4616 b occupies a region of parameter space comparable to, or more extreme than, TOI-561 b, for which JWST

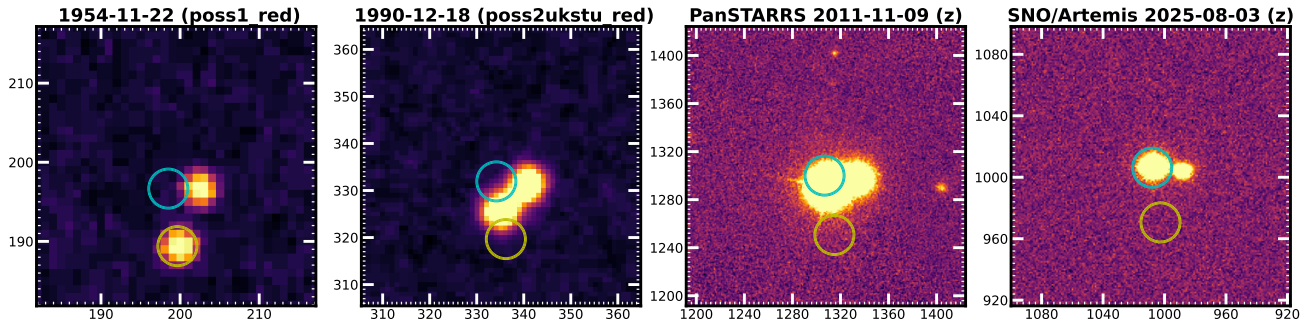


Figure 15. Archival images for TOI-4616. Yellow circles show the position of the star in the earliest image, and blue circles show the position of the star in the most recent images. The target shifted $12.9''$ from 1954 to 2025. These images show that there is no background star blending within the current position of our target and that the nearby source is a background object.

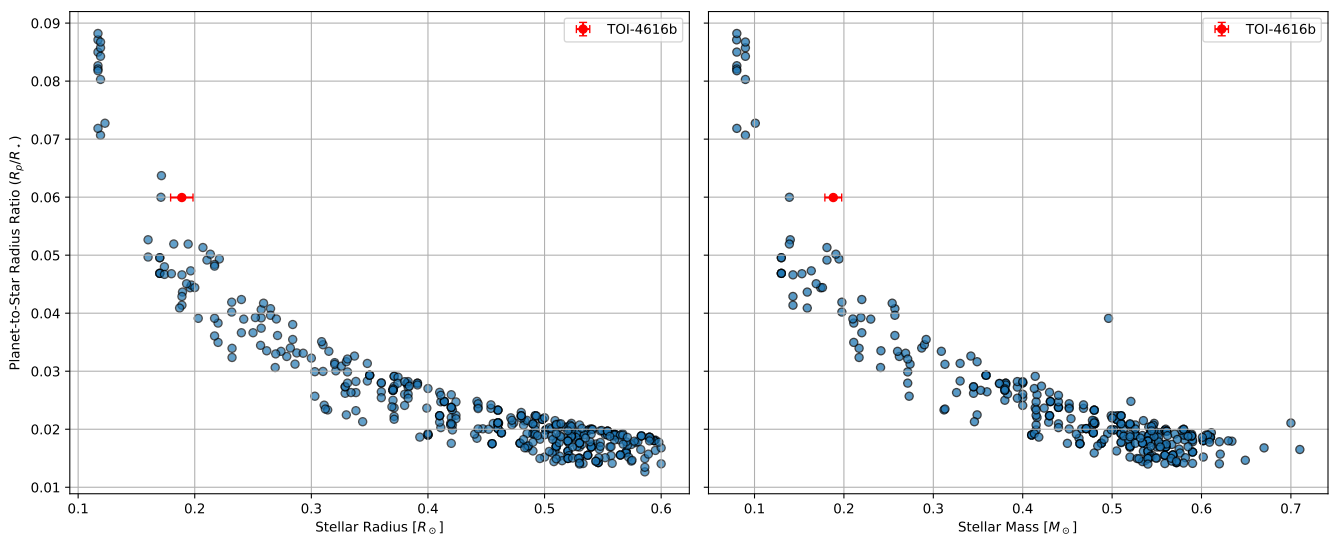


Figure 16. This shows the population of Earth-sized planets around M-dwarfs. In the right panel, we show the population in relation to stellar mass, and on the right, the population related to stellar radius. The red dot in each panel shows the position of TOI-4616 b relative to other planets. The data for the planetary and stellar populations are from the NASA EXOPLANET ARCHIVE accessed on UTC 2025 March 6 (Christiansen 2022).

observations have recently revealed evidence for a substantial atmosphere (Teske et al. 2025). This suggests that the empirical shoreline is not a strict boundary and highlights TOI-4616 b as a stringent test of atmospheric survival under extreme irradiation.

8.3 Atmospheric characterization prospects

We evaluated the suitability of TOI-4616,b for atmospheric characterization using the Transmission Spectroscopy Metric (TSM) and Emission Spectroscopy Metric (ESM) defined by Kempton et al. (2018). Using posterior samples from our joint fit, including contamination corrections, we obtain $TSM = 21.4$ and $ESM = 2.9$.

The transmission spectroscopy metric (TSM; Kempton et al. 2018) lies above the recommended threshold for atmospheric characterization of terrestrial planets ($TSM > 10$ for $R_p < 1.5 R_\oplus$), indicating that transmission spectroscopy with JWST could potentially detect atmospheric features if TOI-4616 b retains a secondary atmosphere (Fig. 18). In contrast, the emission spectroscopy metric (ESM) falls below the recommended threshold for thermal emission detection

($ESM > 7.5$), suggesting that secondary-eclipse observations are unlikely to provide strong constraints on the planet’s atmosphere.

TOI-4616,b therefore emerges as one of the few Earth-sized planets orbiting mid-M dwarfs that remains accessible to JWST transmission spectroscopy. Its combination of extreme irradiation, well-constrained stellar properties, and observational accessibility makes it a valuable benchmark for testing models of atmospheric loss, retention, and replenishment in the terrestrial regime.

Continued photometric and spectroscopic monitoring will refine the ephemeris, enable a future mass measurement, and search for additional companions, further strengthening its role as a reference system for highly irradiated rocky planets.

9 ACKNOWLEDGEMENTS

Some of the observations presented in this paper were carried out at the Observatorio Astronómico Nacional on the Sierra de San Pedro Mártir (OAN-SPM), Baja California, México. This work makes use of observations from the LCOGT network; part of the telescope

Table 3. Joint-fit priors and best-fit parameters for TOI-4616.

Parameter	Prior	Best fit	Description
<i>Planetary parameters</i>			
P_b (d)	$\mathcal{N}(1.5538, 0.0001^2)$	1.55382 ± 0.00001	Orbital period
$T_{0,b}$ (BJD-2457000)	$\mathcal{N}(2684.880363943, 0.05^2)$	2684.88885 ± 0.00034	Mid-transit time
b_0	$\mathcal{U}(0, 1)$	0.80 ± 0.20	Impact parameter
e_b	Fixed	0	Eccentricity
ω_b (deg)	Fixed	90	Arg. of periapsis
<i>Stellar parameters</i>			
ρ_* (ρ_\odot)	$\mathcal{N}(27.9, 2^2)$	30.655 ± 2.700	Stellar density
TESS Band			
μ	$\mathcal{N}(0, 0.001^2)$	0.0001 ± 0.002	TESS-specific parameters mean flux
u_1	$\mathcal{N}(0.32, 0.15^2)$	0.32 ± 0.14	quadratic limb dark
u_2	$\mathcal{N}(0.26, 0.15^2)$	0.29 ± 0.14	linear limb dark
d	$\mathcal{U}(4.54 \times 10^{-5}, 1.35 \times 10^{-1})$	0.0026 ± 0.0005	Transit depth
SAINT-EX I+z			
μ	$\mathcal{N}(0, 0.001^2)$	0.0000 ± 0.0020	SAINT-EX-specific parameters mean flux
u_1	$\mathcal{N}(0.29, 0.15^2)$	0.33 ± 0.14	quadratic limb dark
u_2	$\mathcal{N}(0.26, 0.15^2)$	0.29 ± 0.14	linear limb dark
d	$\mathcal{U}(1.2 \times 10^{-4}, 1.4 \times 10^{-1})$	0.0031 ± 0.0005	Transit depth
MuSCAT3 Ip			
μ	$\mathcal{N}(0, 0.001^2)$	0.0000 ± 0.0020	Ip-specific parameters mean flux
u_1	$\mathcal{N}(0.32, 0.15^2)$	0.37 ± 0.14	quadratic limb dark
u_2	$\mathcal{N}(0.27, 0.15^2)$	0.31 ± 0.14	linear limb dark
d	$\mathcal{U}(3.35 \times 10^{-4}, 5.00 \times 10^{-2})$	0.0033 ± 0.0007	Transit depth
MuSCAT3 Rp			
μ	$\mathcal{N}(0, 0.001^2)$	0.0000 ± 0.0020	Rp-specific parameters mean flux
u_1	$\mathcal{N}(0.48, 0.15^2)$	0.44 ± 0.12	quadratic limb dark
u_2	$\mathcal{N}(0.24, 0.15^2)$	0.26 ± 0.13	linear limb dark
d	$\mathcal{U}(1.2 \times 10^{-4}, 1.4 \times 10^{-1})$	0.0036 ± 0.0004	Transit depth
MuSCAT3 Gp			
μ	$\mathcal{N}(0, 0.001^2)$	0.0000 ± 0.0020	Gp-specific parameters mean flux
u_1	$\mathcal{N}(0.61, 0.15^2)$	$0.63^{+0.13}_{-0.12}$	quadratic limb dark
u_2	$\mathcal{N}(0.29, 0.15^2)$	0.31 ± 0.13	linear limb dark
d	$\mathcal{U}(1.2 \times 10^{-4}, 5.0 \times 10^{-2})$	0.0031 ± 0.0004	Transit depth
MuSCAT3 z-short			
μ	$\mathcal{N}(0, 0.001^2)$	0.0000 ± 0.002	Z-Short-specific parameters mean flux
u_1	$\mathcal{N}(0.27, 0.15^2)$	0.28 ± 0.14	quadratic limb dark
u_2	$\mathcal{N}(0.26, 0.15^2)$	0.26 ± 0.15	linear limb dark
d	$\mathcal{U}(1.2 \times 10^{-4}, 5.0 \times 10^{-2})$	$0.0034^{+0.0011}_{-0.0016}$	Transit depth
LCO-Teid ip			
mean	$\mathcal{N}(0, 0.001^2)$	0.0000 ± 0.0020	Ip-specific parameters mean flux
u_1	$\mathcal{N}(0.32, 0.15^2)$	0.27 ± 0.14	quadratic limb dark
u_2	$\mathcal{N}(0.27, 0.15^2)$	0.23 ± 0.14	linear limb dark
d	$\mathcal{U}(1.2 \times 10^{-4}, 5.0 \times 10^{-2})$	0.0030 ± 0.0006	Transit depth
SAINT-EX ip			
mean	$\mathcal{N}(0, 0.001^2)$	0.0000 ± 0.0020	ip-specific parameters mean flux
u_1	$\mathcal{N}(0.32, 0.15^2)$	0.42 ± 0.12	quadratic limb dark
u_2	$\mathcal{N}(0.27, 0.15^2)$	0.35 ± 0.13	linear limb dark
d	$\mathcal{U}(4.5 \times 10^{-5}, 5.0 \times 10^{-2})$	0.0034 ± 0.0003	Transit depth

Note. $\mathcal{U}(a, b)$: uniform prior from a to b ; $\mathcal{N}(\mu, \sigma^2)$: normal prior; quadratic limb darkening priors were calculated using the LDTK package (Parviainen & Aigrain 2015). We took t_0 at the midpoint of each dataset to remove the strong covariance between t_0 and the period (Eastman et al. 2013; Agol et al. 2005).

time was granted by NOIRLab through the Mid-Scale Innovations Program (MSIP), funded by the NSF. This research also made use of the Exoplanet Follow-up Observation Program (ExoFOP-TESS; DOI: 10.26134/ExoFOP5), operated by the California Institute of Technology under contract with NASA's Exoplanet Exploration Program. Computational work was performed on the UBELIX cluster at the University of Bern, and we thank the high-performance computing team for their support.

We acknowledge support from the Swiss National Science Foundation (SNSF) through the SPIRIT project IZSTZ0.216537 and through the National Centre for Competence in Research Planets. Additional

institutional support was provided by the Centre for Space and Habitability (CSH) at the University of Bern. Funding for the TESS mission is provided by NASA's Science Mission Directorate; KAC and CNW acknowledge support via subaward s3449 from MIT.

YGMC, AK, IPF, and MPM acknowledge partial support from UNAM PAPIIT-IG101224. B.-O. D. acknowledges support from the Swiss State Secretariat for Education, Research and Innovation (SERI) under contract MB22.00046. HPO acknowledges support from the SNSF through PlanetS grants 51NF40_182901 and 51NF40_205606. KB acknowledges support from the European Union (ERC Advanced Grant SUBSTELLAR, GA 101054354). This work also received

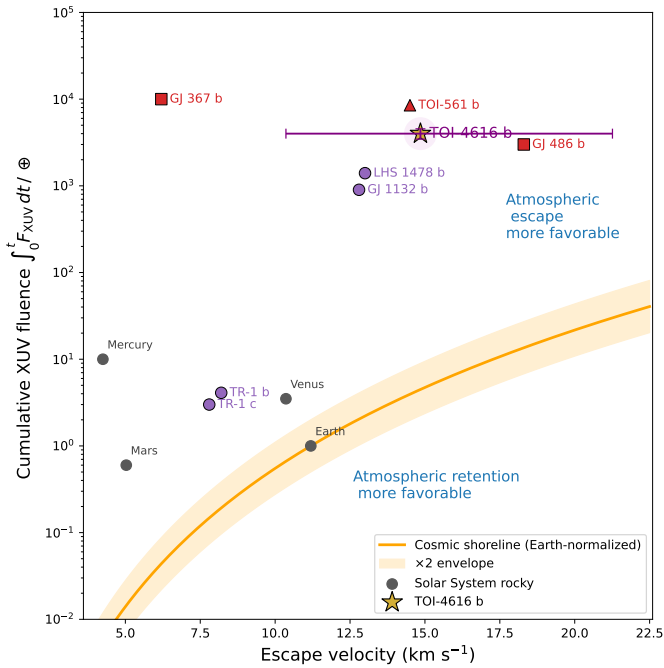


Figure 17. Location of TOI-4616 b in the cumulative XUV fluence–escape velocity plane, shown in the context of the empirical cosmic shoreline. The orange curve and shaded region indicate the Solar-System-derived cosmic shoreline relation (Zahnle & Catling 2017) and its uncertainty envelope, separating regimes where atmospheres are expected to be retained (below) or efficiently eroded (above). Solar System rocky planets are shown for reference. TOI-4616 b (purple star) lies well above the shoreline, in a region where atmospheric survival is nominally disfavoured, at cumulative XUV fluence comparable to or exceeding that of TOI-561 b. The location of TOI-561 b—despite recent JWST evidence for a substantial atmosphere—highlights that the cosmic shoreline is not a strict boundary and motivates TOI-4616 b as a stringent test case for atmospheric escape and survival under extreme irradiation.

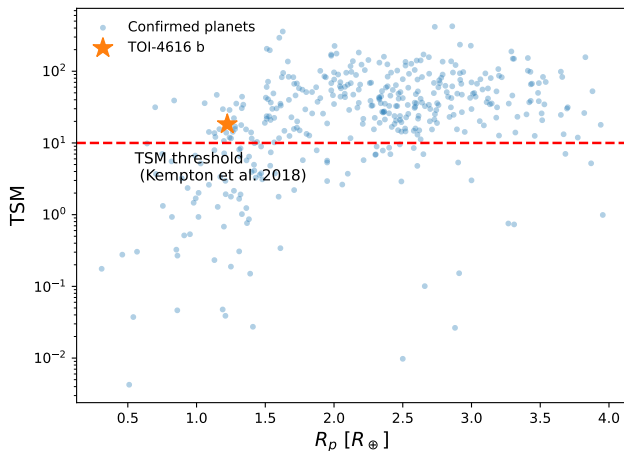


Figure 18. TSM as a function of planetary radius for confirmed transiting planets orbiting M dwarfs. Blue points show the known population compiled from the NASA Exoplanet Archive, accessed on UTC 2026 February 2. The orange star marks TOI-4616 b. The planet lies above the nominal TSM threshold for transmission spectroscopy of terrestrial planets, indicating that atmospheric features could be detectable with JWST if a secondary atmosphere is present.

support from NASA under Agreement 80NSSC21K0593 (“Alien Earths”) and benefited from collaborations within the NExSS research coordination network. Support from the ERC Synergy Grant REVEAL (No. 101118581) is also acknowledged.

F. M. acknowledges the financial support from the Agencia Estatal de Investigación del Ministerio de Ciencia, Innovación y Universidades (MCIU/AEI) through grant PID2023-152906NA-I00.

The ULiege contribution to SPECULOOS has received funding from the European Research Council (grant 336480/SPECULOOS), the Balzan and Francqui Foundations, the Belgian F.R.S.-FNRS (grant T.0109.20), the University of Liège, and the Wallonia-Brussels Federation. M. Gillon is F.R.S.-FNRS Research Director. The Wallonian Region is thanked for funding the SPECULOOS-North/Artemis telescope. J.d.W. and MIT gratefully acknowledge financial support from the Heising-Simons Foundation, Dr. and Mrs. Colin Masson and Dr. Peter A. Gilman for Artemis, the first telescope of the SPECULOOS network situated in Tenerife, Spain.

This article is based on observations made with the MuSCAT2 instrument, developed by ABC, at Telescopio Carlos Sánchez operated on the island of Tenerife by the IAC in the Spanish Observatorio del Teide. This work is partly financed by the Spanish Ministry of Economics and Competitiveness through grants PGC2018-098153-B-C31. This work is partly supported by JSPS KAKENHI Grant Numbers JP24H00017, JP24K00689, and JSPS Bilateral Program Number JPJSBP120249910.

This paper is based on observations made with the MuSCAT instruments developed by the Astrobiology Center (ABC), the University of Tokyo, and LCOGT. MuSCAT3 was developed with support from JSPS KAKENHI (JP18H05439) and JST PRESTO (JPMJPR1775). MuSCAT2 observations were obtained at the Telescopio Carlos Sánchez operated by the IAC at the Observatorio del Teide. Additional support was provided by MCIN/AEI/ERDF projects PID2021-125627OB-C32 and PID2024-158486OB-C32, by the Severo Ochoa Centre of Excellence program, and by JSPS KAKENHI grants JP24H00017 and JP24K00689. F.M. acknowledges support from MCIU/AEI grant PID2023-152906NA-I00.

Observations at the Infrared Telescope Facility were conducted as Visiting Astronomers; the IRTF is operated by the University of Hawai‘i under contract 80HQTR24DA010 with NASA.

DATA AVAILABILITY

The data underlying this article are publicly available. TESS photometry is available from the Mikulski Archive for Space Telescopes (MAST). Ground-based photometry is available via the Exoplanet Follow-up Observing Program (ExoFOP–TESS). Reduced light curves and analysis scripts used in this work are available from the corresponding author upon reasonable request.

REFERENCES

- Agol E., Steffen J., Sari R., Clarkson W., 2005, *Monthly Notices of the Royal Astronomical Society*, 359, 567
- Aller A., Lillo-Box J., Jones D., Miranda L. F., Forteza S. B., 2020, *A&A*, 635, A128
- Artigau É., et al., 2024, in *Ground-based and Airborne Instrumentation for Astronomy X*, pp 71–87
- Bochanski J. J., West A. A., Hawley S. L., Covey K. R., 2007, *AJ*, 133, 531
- Bradley L., et al., 2020, Zenodo
- Bray J., Kolb U., Mills S., 2025, *Monthly Notices of the Royal Astronomical Society*, 540, 2578

- Brown T. M., et al., 2013, *PASP*, 125, 1031
- Burdanov A. Y., et al., 2022, *PASP*, 134, 105001
- Burgasser A. J., Splat Development Team 2017, in *Astronomical Society of India Conference Series*. pp 7–12 ([arXiv:1707.00062](https://arxiv.org/abs/1707.00062))
- Caldirolì A., Haardt F., Gallo E., Spinelli R., Malsky I., Rauscher E., 2021, *Astronomy & Astrophysics*, 655, A30
- Chabrier G., Johansen A., Janson M., Rafikov R., 2014, arXiv preprint [arXiv:1401.7559](https://arxiv.org/abs/1401.7559)
- Chachan Y., Lee E. J., 2023, *The Astrophysical Journal Letters*, 952, L20
- Chen J., Kipping D., 2017, *The Astrophysical Journal*, 834, 17
- Christiansen J. L., 2022, *Nature Astronomy*, 6, 516
- Collins K. A., Kielkopf J. F., Stassun K. G., Hessman F. V., 2017a, *AJ*, 153, 77
- Collins K. A., Kielkopf J. F., Stassun K. G., Hessman F. V., 2017b, *The Astronomical Journal*, 153, 77
- Crossfield I. J. M., Ciardi D. R., Petigura E. A., et al., 2016, *The Astrophysical Journal Supplement Series*, 226, 7
- Cushing M. C., Vacca W. D., Rayner J. T., 2004, *PASP*, 116, 362
- Cushing M. C., Rayner J. T., Vacca W. D., 2005, *ApJ*, 623, 1115
- Delchambre L., 2015, *Monthly Notices of the Royal Astronomical Society*, 446, 3545
- Delrez L., et al., 2018a, in *Ground-based and airborne telescopes VII*. pp 446–466
- Delrez L., et al., 2018b, in Marshall H. K., Spyromilio J., eds, *Society of Photo-Optical Instrumentation Engineers (SPIE) Conference Series Vol. 10700, Ground-based and Airborne Telescopes VII*. p. 1070011 ([arXiv:1806.11205](https://arxiv.org/abs/1806.11205)), doi:10.1117/12.2312475
- Demory B.-O., et al., 2020, *A&A*, 642, A49
- Dévora-Pajares M., Pozuelos F. J., 2022, *MATRIX: Multi-phAse Transits Recovery from Injected exoplanets*, Zenodo, doi:10.5281/zenodo.6570831
- Dévora-Pajares M., Pozuelos F. J., Thuillier A., Timmermans M., Van Grootel V., Bonidie V., Mota L. C., Suárez J. C., 2024, *MNRAS*, 532, 4752
- Donati J.-F., et al., 2018, in *Handbook of Exoplanets*. Springer, pp 1–27
- Douglas S. T., et al., 2014, *ApJ*, 795, 161
- Dransfield G., et al., 2024, *MNRAS*, 527, 35
- Dressing C. D., Charbonneau D., 2013, *The Astrophysical Journal*, 767, 95
- Eastman J., Gaudi B. S., Agol E., 2013, *Publications of the Astronomical Society of the Pacific*, 125, 83
- Eylen V. V., et al., 2019, *The Astronomical Journal*, 157, 61
- Foreman-Mackey D., Hogg D. W., Lang D., Goodman J., 2013, *Publications of the Astronomical Society of the Pacific*, 125, 306
- Foreman-Mackey D., Agol E., Ambikasaran S., Angus R., 2017, *The Astronomical Journal*, 154, 220
- Gaia Collaboration et al., 2021, *A&A*, 649, A1
- Gaia Collaboration et al., 2023, *A&A*, 674, A1
- García L. J., Timmermans M., Pozuelos F. J., Ducrot E., Gillon M., Delrez L., Wells R. D., Jehin E., 2022, *MNRAS*, 509, 4817
- Ghachoui M., et al., 2024, *A&A*, 690, A263
- Giacalone S. A., 2023, PhD thesis, University of California, Berkeley
- Giacalone S., et al., 2020, *The Astronomical Journal*, 161, 24
- Giacalone S., et al., 2021, *AJ*, 161, 24
- Gizis J. E., 1997, *AJ*, 113, 806
- Gratton R., 2025, *Rendiconti Lincei. Scienze Fisiche e Naturali*, pp 1–16
- Hadden S., Lithwick Y., 2014, *The Astrophysical Journal*, 787, 80
- Hamuy M., Walker A. R., Suntzeff N. B., Gigoux P., Heathcote S. R., Phillips M. M., 1992, *PASP*, 104, 533
- Hamuy M., Suntzeff N. B., Heathcote S. R., Walker A. R., Gigoux P., Phillips M. M., 1994, *PASP*, 106, 566
- Hippke M., David T. J., Mulders G. D., Heller R., 2019, *AJ*, 158, 143
- Howell S. B., Everett M. E., Sherry W., Horch E., Ciardi D. R., 2011, *The Astronomical Journal*, 142, 19
- Howell S. B., Matson R. A., Ciardi D. R., Everett M. E., Livingston J. H., Scott N. J., Horch E. P., Winn J. N., 2021, *The Astronomical Journal*, 161, 164
- Husser T.-O., Wende-von Berg S., Dreizler S., Homeier D., Reiners A., Barman T., Hauschildt P. H., 2013, *A&A*, 553, A6
- Jehin E., et al., 2018, *The Messenger*, 174, 2
- Jensen E., 2013, *Tapir: A web interface for transit/eclipse observability*, *Astrophysics Source Code Library (ascl:1306.007)*
- Ji X., Chatterjee R. D., Coy B. P., Kite E., 2025, *The Astrophysical Journal*, 992, 198
- Karnavas A. A., 2024, PhD thesis, Universidade do Porto (Portugal)
- Kempton E. M.-R., et al., 2018, *Publications of the Astronomical Society of the Pacific*, 130, 114401
- Kesseli A. Y., et al., 2019, *AJ*, 157, 63
- Kochoska A., Mowlavi N., Prša A., Lecoeur-Taïbi I., Holl B., Rimoldini L., Süveges M., Eyer L., 2017, *Astronomy & Astrophysics*, 602, A110
- Kreidberg L., 2015, *Publications of the Astronomical Society of the Pacific*, 127, 1161
- Lang D., Hogg D. W., Mierle K., Blanton M., Roweis S., 2010, *The astronomical journal*, 139, 1782
- Lépine S., Rich R. M., Shara M. M., 2003, *AJ*, 125, 1598
- Lépine S., Hilton E. J., Mann A. W., Wilde M., Rojas-Ayala B., Cruz K. L., Gaidos E., 2013, *AJ*, 145, 102
- Lester K. V., et al., 2021, *The Astronomical Journal*, 162, 75
- Libby-Roberts J. E., et al., 2022, *The Astronomical Journal*, 164, 59
- Lightkurve Collaboration et al., 2018, *Lightkurve: Kepler and TESS time series analysis in Python*, *Astrophysics Source Code Library (ascl:1812.013)*
- Lindgren S., Heiter U., Seifahrt A., 2016, *Astronomy & Astrophysics*, 586, A100
- Livingston J. H., Crossfield I. J. M., Petigura E. A., et al., 2018, *The Astronomical Journal*, 156, 277
- Mandel K., Agol E., 2002, *The Astrophysical Journal*, 580, L171
- Mann A. W., Brewer J. M., Gaidos E., Lépine S., Hilton E. J., 2013a, *AJ*, 145, 52
- Mann A. W., Brewer J. M., Gaidos E., Lépine S., Hilton E. J., 2013b, *AJ*, 145, 52
- Mann A. W., Feiden G. A., Gaidos E., Boyajian T., von Braun K., 2015, *ApJ*, 804, 64
- Mann A. W., et al., 2019, *ApJ*, 871, 63
- Mantovan G., et al., 2022, *Monthly Notices of the Royal Astronomical Society*, 516, 4432
- Martín E. L., Delfosse X., Basri G., Goldman B., Forveille T., Zapatero Osorio M. R., 1999, *AJ*, 118, 2466
- Mayo A. W., Vanderburg A., Latham D. W., et al., 2018, *The Astronomical Journal*, 155, 136
- McCully C., Volgenau N. H., Harbeck D.-R., Lister T. A., Saunders E. S., Turner M. L., Siiverv R. J., Bowman M., 2018, in Guzman J. C., Ibsen J., eds, *Society of Photo-Optical Instrumentation Engineers (SPIE) Conference Series Vol. 10707, Software and Cyberinfrastructure for Astronomy V*. p. 107070K ([arXiv:1811.04163](https://arxiv.org/abs/1811.04163)), doi:10.1117/12.2314340
- Meni-Gallardo P., Pallé E., 2025, arXiv preprint [arXiv:2508.12865](https://arxiv.org/abs/2508.12865)
- Miller J. S., Stone R. P. S., 1994, *Technical Report 66, The Kast Double Spectrograph*. University of California Lick Observatory Technical Reports
- Misener W., Schlichting H. E., 2021, *Monthly Notices of the Royal Astronomical Society*, 503, 5658
- Mislis D., Schröter S., Schmitt J., Cordes O., Reif K., 2010, *Astronomy & Astrophysics*, 510, A107
- Mistry P., et al., 2023, *The Astronomical Journal*, 166, 9
- Narita N., et al., 2019, *Journal of Astronomical Telescopes, Instruments, and Systems*, 5, 015001
- Narita N., et al., 2020, in *Society of Photo-Optical Instrumentation Engineers (SPIE) Conference Series*. p. 114475K, doi:10.1117/12.2559947
- Neckel H., 1995, *solar Physics*, 156, 7
- Palle E., et al., 2025, *Astronomy & Astrophysics*, 697, A31
- Parviainen H., Aigrain S., 2015, *Monthly Notices of the Royal Astronomical Society*, 453, 3821
- Parviainen H., et al., 2019, *Astronomy & Astrophysics*, 630, A89
- Passegger V., et al., 2022, *Astronomy & Astrophysics*, 658, A194
- Pedersen P. P., Degen D., García L., Zúñiga-Fernández S., Sebastian D., Queloz D., 2023, *Astra Observatory Control Software*, <https://github.com/ppp-one/astra>
- Peláez-Torres A., et al., 2024, *Astronomy & Astrophysics*, 690, A62
- Pozuelos F. J., et al., 2020, *A&A*, 641, A23
- Pozuelos F. J., et al., 2023, *A&A*, 672, A70
- Prša A., et al., 2011, *The Astronomical Journal*, 141, 83

- Rayner J. T., Toomey D. W., Onaka P. M., Denault A. J., Stahlberger W. E., Vacca W. D., Cushing M. C., Wang S., 2003, *PASP*, **115**, 362
- Rayner J. T., Cushing M. C., Vacca W. D., 2009, *ApJS*, **185**, 289
- Reid I. N., Hawley S. L., Gizis J. E., 1995, *AJ*, **110**, 1838
- Ricker G. R., et al., 2015, *Journal of Astronomical Telescopes, Instruments, and Systems*, **1**, 014003
- Riddick F. C., Roche P. F., Lucas P. W., 2007, *MNRAS*, **381**, 1067
- Rojas-Ayala B., Covey K. R., Muirhead P. S., Lloyd J. P., 2012, *ApJ*, **748**, 93
- Schanche N., et al., 2022, *A&A*, **657**, A45
- Schöfer P., 2021, PhD thesis, Dissertation, Göttingen, Georg-August Universität, 2021
- Scott N. J., Howell S. B., Horch E. P., Everett M. E., 2018, *Publications of the Astronomical Society of the Pacific*, **130**, 054502
- Sebastian D., et al., 2020, in *Ground-based and airborne telescopes viii*. pp 431–446
- Sebastian D., et al., 2021a, *Astronomy & Astrophysics*, **645**, A100
- Sebastian D., et al., 2021b, *A&A*, **645**, A100
- Shporer A., et al., 2014, *The Astrophysical Journal*, **788**, 92
- Skrutskie M. F., et al., 2006, *AJ*, **131**, 1163
- Sprague D., et al., 2022, *AJ*, **163**, 152
- Stassun K. G., Torres G., 2016, *AJ*, **152**, 180
- Stassun K. G., Torres G., 2018, *ApJ*, **862**, 61
- Stassun K. G., Torres G., 2021, *ApJ*, **907**, L33
- Stassun K. G., Collins K. A., Gaudi B. S., 2017, *AJ*, **153**, 136
- Stassun K. G., et al., 2018, *The Astronomical Journal*, **156**, 102
- Suárez Mascareño A., Rebolo R., González Hernández J., Esposito M., 2017, *Monthly Notices of the Royal Astronomical Society*, **468**, 4772
- Teske J. K., et al., 2025, arXiv preprint arXiv:2509.17231
- Wells R. D., et al., 2021, *A&A*, **653**, A97
- West A. A., Hawley S. L., Bochanski J. J., Covey K. R., Reid I. N., Dhital S., Hilton E. J., Masuda M., 2008, *AJ*, **135**, 785
- Yalçinkaya S., et al., 2025, arXiv e-prints, p. arXiv:2509.05038
- Zahnle K. J., Catling D. C., 2017, *The Astrophysical Journal*, **843**, 122
- Ziegler C., Tokovinin A., Latiolais M., Briceño C., Law N., Mann A. W., 2021, *The Astronomical Journal*, **162**, 192
- Zúñiga-Fernández S., et al., 2025, arXiv e-prints, p. arXiv:2508.14176

APPENDIX A: PAIR-WISE R_p/R_* DIFFERENCE DISTRIBUTIONS BETWEEN DATASETS

We present the distribution of radius ratio differences between datasets, and show how these deviate from zero.

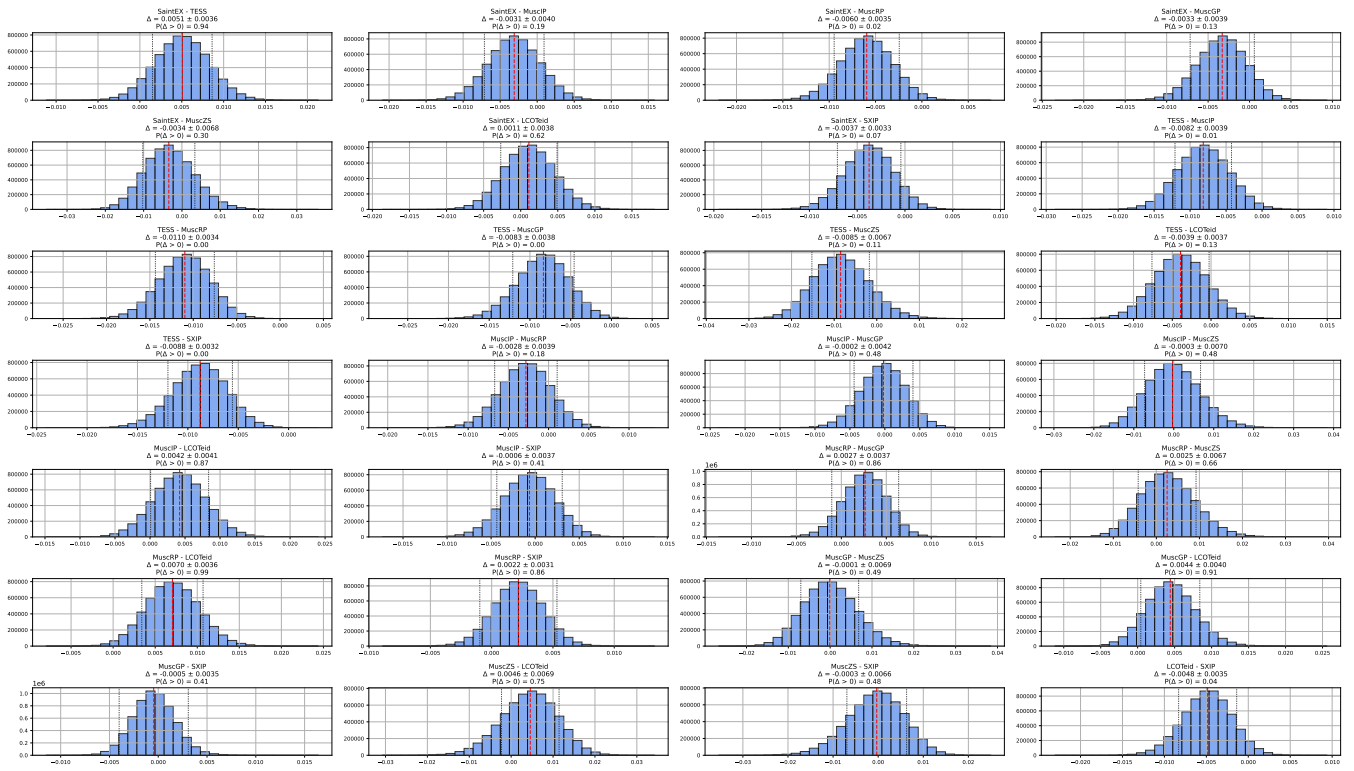


Figure A1. The plots above are the pairwise distributions of the difference in the planet-star radius ratios for all the light curves in the joint fit. The broken red vertical lines indicate the median of each distribution. These provide a picture of how much the median differs from zero. These plots will indicate a measure of the robustness in the planet-to-star radius ratio calculations. We also show the error propagation in the fits, indicating that the median in each distribution lies within the error bars.

APPENDIX B: STATISTICAL SIGNIFICANCE OF R_p/R_\star DIFFERENCES

Table B1. Bayesian classification of R_p/R_* differences for 28 instrument pairs

Pair	Δ	σ	$P(\Delta > 0)$	Z_{Freq}	Z_{Bayes}	Significance Class
SAINT-EX - TESS	0.0050	0.0034	0.950	1.7353	0.9900	Significant ($\Delta > 0$)
SAINT-EX - MuscatIP	0.0030	0.0037	0.9190	1.0541	0.8380	Not significant
SAINT-EX - MuscatRP	0.0058	0.0032	0.9910	1.8125	0.9820	Significant ($\Delta > 0$)
SAINT-EX - MuscatGP	0.0031	0.0034	0.9140	0.9118	0.8280	Not significant
SAINT-EX - LCO+Teid	0.0010	0.0026	0.6240	0.3846	0.2480	Not significant
SAINT-EX - SXIP	0.0030	0.0030	0.9270	1.0000	0.8540	Not significant
SAINT-EX - MuscatZs	-0.0035	0.0068	0.3000	0.515	0.5240	Not significant
TESS - MuscatIP	-0.0060	0.0037	0.0100	1.6216	-0.9800	Significant ($\Delta < 0$)
TESS - MuscatRP	-0.0109	0.0031	0.0000	2.7949	-1.0000	Significant ($\Delta < 0$)
TESS - MuscatGP	-0.0048	0.0034	0.0100	1.4118	-0.9800	Significant ($\Delta < 0$)
TESS - LCO+Teid	-0.0040	0.0026	0.1120	1.5385	-0.7760	Not significant
TESS - SXIP	-0.0067	0.0029	0.0000	2.3103	-1.0000	Significant ($\Delta < 0$)
TESS - MuscatZs	-0.0005	0.0058	0.1100	0.0862	-0.7800	Not significant
MuscatIP - MuscatRP	0.0020	0.0035	0.1800	0.5714	-0.6400	Not significant
MuscatIP - MuscatGP	0.0001	0.0037	0.4900	0.0270	-0.0200	Not significant
MuscatIP - LCO+Teid	0.0040	0.0039	0.8600	1.2564	0.7200	Not significant
MuscatIP - MuscatZS	-0.0005	0.0070	0.4700	0.07142	-0.0600	Not significant
MuscatIP - SXIP	-0.0026	0.0034	0.4100	0.7647	-0.1800	Not significant
MuscatRP - MuscatGP	0.0028	0.0031	0.8800	0.9032	0.7600	Not significant
MuscatRP - MuscatZS	0.0024	0.0067	0.4700	0.36	-0.075	Not significant
MuscatRP - LCO+Teid	0.0069	0.0034	0.6600	2.0294	0.3200	Not significant
MuscatRP - SXIP	-0.0022	0.0027	0.3420	0.8148	-0.3160	Not significant
MuscatGP - MuscatZs	0.0040	0.0068	0.4700	0.5882	-0.0600	Not significant
MuscatGP - SXIP	-0.0006	0.0029	0.3800	0.2069	-0.2400	Not significant
MuscatGP - LCO+Teid	0.0041	0.0036	0.9100	1.1111	0.8200	Not significant
MuscatZs - LCO+Teid	0.0045	0.0070	0.7500	0.0714	0.5000	Not significant
MuscatZs - SXIP	-0.0045	0.0096	0.4900	0.4688	-0.0200	Not significant
LCO+Teid - SXIP	-0.0040	0.0032	0.0900	1.2500	-0.8200	Not significant

APPENDIX C: CORNER PLOTS

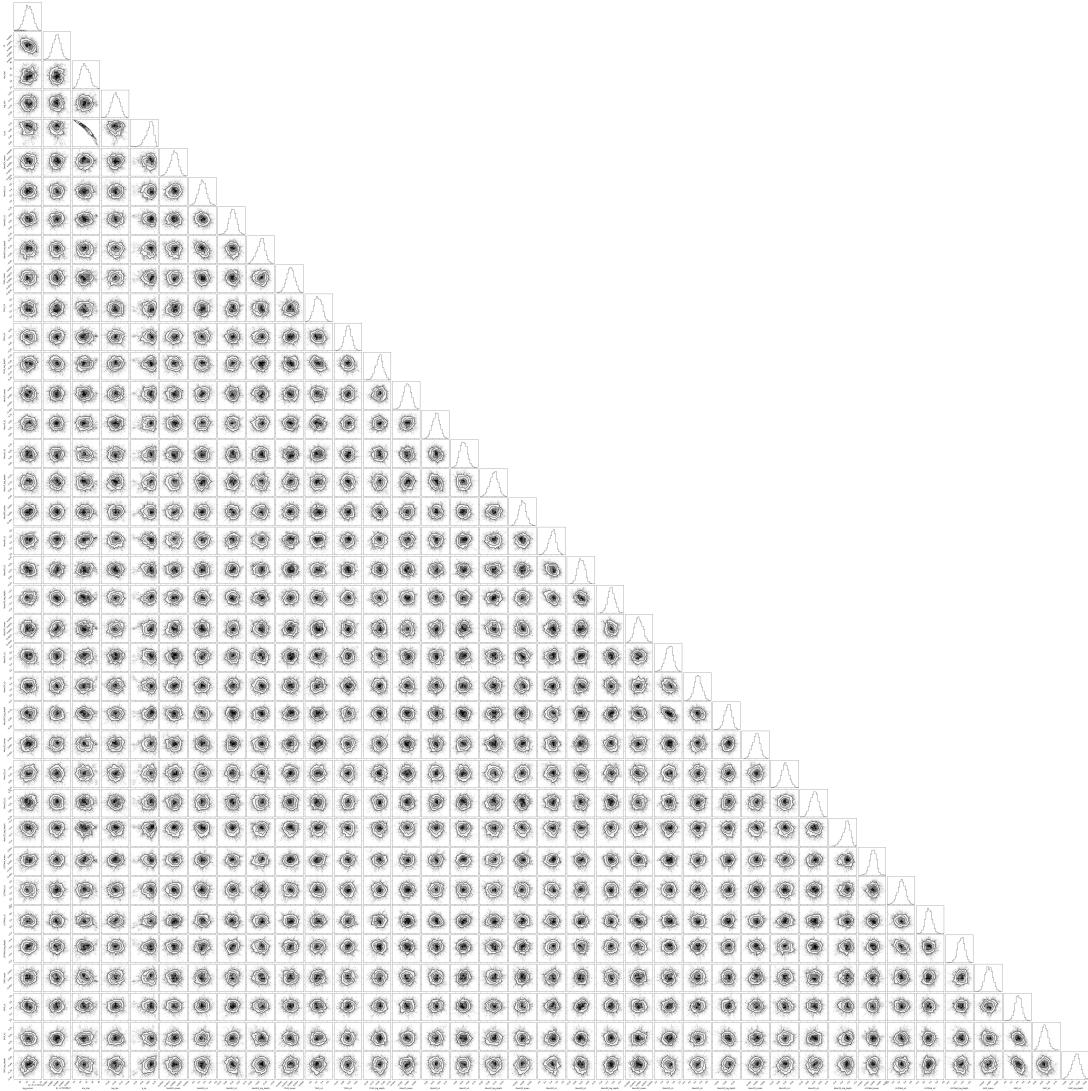


Figure C1. Corner plots for datasets from four instruments (TESS, SAINT-EX, LCO-Teid, and Muscat3- four filters) in five different filters (I+Z, R', G', I', and Z-short). The first correlation in the upper left corner of the plot is that between the mid-transit time and the log of the period. To prevent a very strong correlation between the period and mid-transit time, we placed a prior at the mid point of each dataset. The Calculations that generated these corner plots were carried out on the University of Bern Linux Cluster (UBELIX)

APPENDIX D: INSTELLATION AND EQUILIBRIUM TEMPERATURE

APPENDIX E: MUSCAT2 DATA

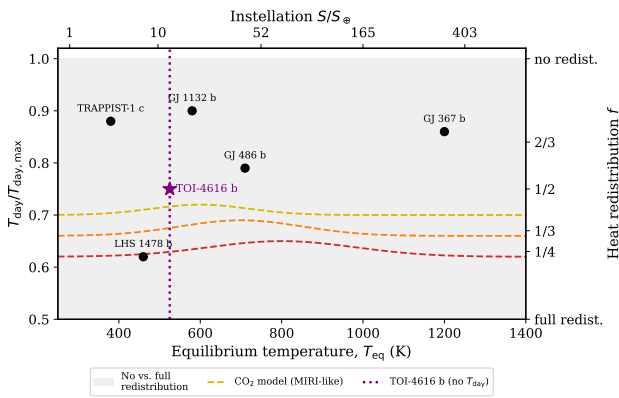


Figure D1. Equilibrium temperature and irradiation diagram illustrating atmospheric heat redistribution regimes for short-period exoplanets. The left axis shows the ratio of dayside temperature to the maximum equilibrium temperature, $T_{\text{day}}/T_{\text{eq,max}}$, while the right axis gives the corresponding heat redistribution factor f . Coloured curves represent theoretical circulation models spanning full to negligible heat redistribution. Black symbols indicate benchmark planets with measured thermal properties. The position of TOI-4616 b (purple star) is shown based on its equilibrium temperature assuming zero Bond albedo. The diagram illustrates the expected range of day–night heat redistribution efficiencies predicted by atmospheric circulation models, and efficient heat redistribution. No direct constraint on the dayside temperature is currently available.

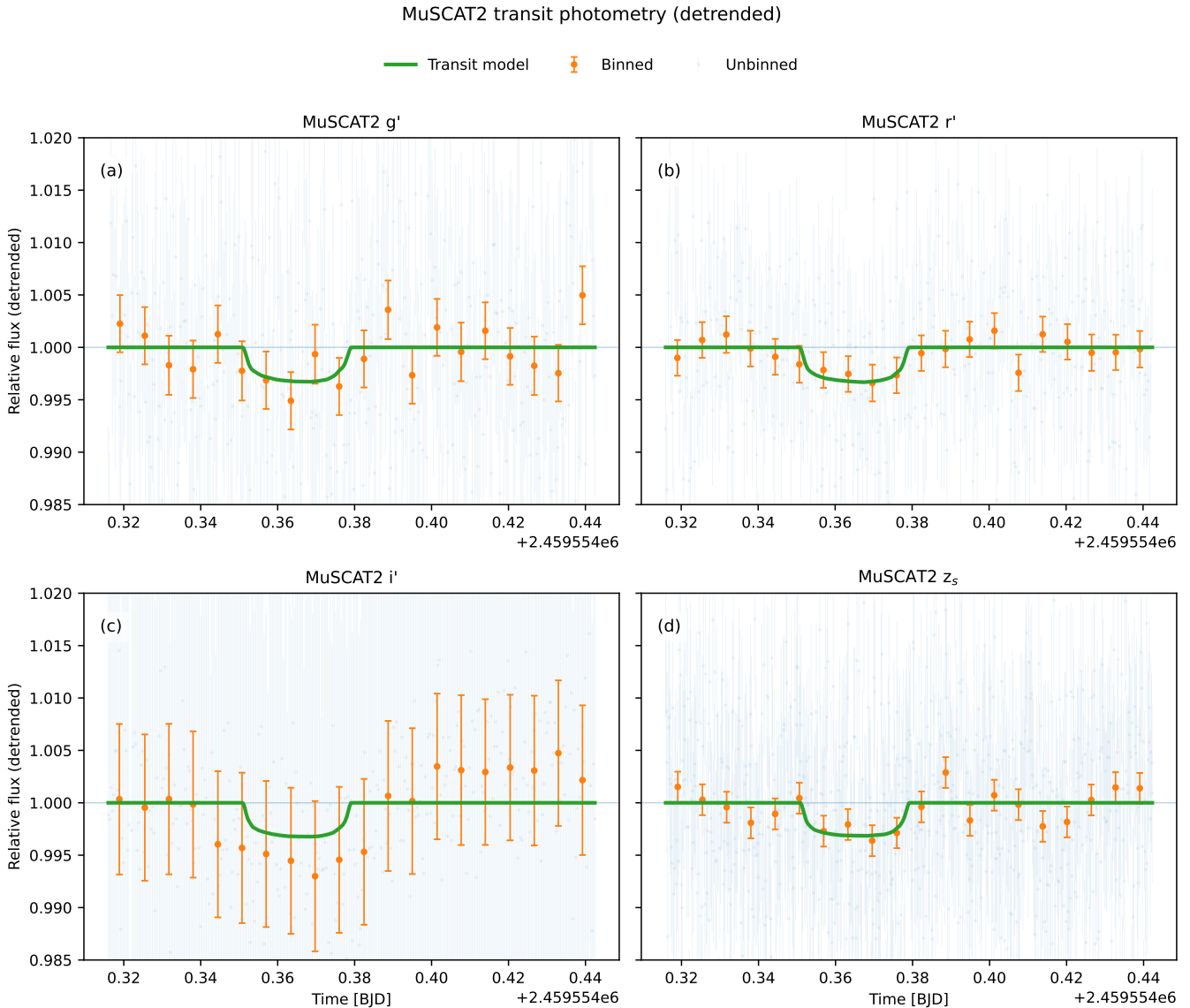


Figure E1. MuSCAT2 g' , r' , i' and z_s light curves, detrended with the quasi-periodic Gaussian Process model from the joint fit. Blue points show the raw detrended photometry, orange points are binned in time, and the green line indicates the best-fitting transit model. Although the individual MuSCAT2 light curves are noisy, the GP detrending recovers a coherent transit depth in each band that is consistent with the global solution from TESS and higher-S/N ground-based instruments, indicating that MuSCAT2 provides a useful consistency check on the planetary interpretation.

APPENDIX F: TRANSIT TIMING ANALYSIS

Transit Timing Variations (TTVs) can reveal additional non-transiting companions through deviations from a strictly linear ephemeris. To search for such signals in TOI-4616,b, we measured individual mid-transit times for both the TESS and ground-based light curves.

For each transit epoch, we performed an independent fit in which the transit shape parameters (depth, duration, and impact parameter) were fixed to the values obtained from the global joint solution. Only the mid-transit time $T_{0,i}$ and a local baseline model were allowed to vary. The observed-minus-calculated residuals were then computed as

$$(O - C)_i = T_{0,i} - (T_0 + N_i P), \quad (\text{F1})$$

where T_0 and P are the reference epoch and orbital period from the global fit, and N_i is the integer transit number.

Figure F2 presents the TESS-only timing residuals. The $(O - C)$ values scatter around zero and are consistent with the uncertainties of the individual timing measurements. No coherent periodic signal or systematic drift relative to a linear ephemeris is detected within the available time baseline.

The same procedure was applied to the ground-based transits (SAINT-EX and other facilities), using only fully covered events. The resulting ground-based timing residuals, shown in Fig. F2, are likewise consistent with the linear ephemeris within their larger uncertainties.

We therefore find no statistically significant evidence for transit timing variations in TOI-4616,b. While low-amplitude perturbations or long-period dynamical effects cannot be excluded below the current timing precision, the available data do not indicate the presence of additional planets detectable through TTVs.

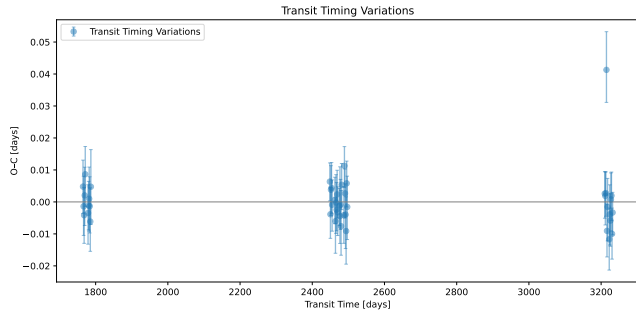


Figure F1. TESS-only transit timing residuals for TOI-4616,b relative to the linear ephemeris from the global fit. Error bars represent the uncertainties from the individual timing fits. The residuals are consistent with zero within uncertainties.

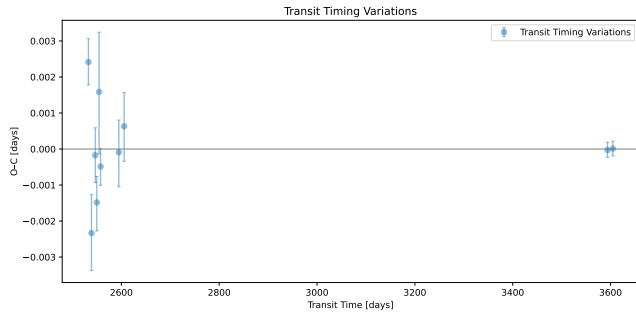


Figure F2. Ground-based transit timing residuals for TOI-4616,b derived from individual event fits. The timings are consistent with the linear ephemeris within the larger uncertainties of the ground-based data.

This paper has been typeset from a $\text{\TeX}/\text{\LaTeX}$ file prepared by the author.